

Testing General Relativity with LISA including Spin Precession and Higher Harmonics in the Waveform

Cédric Huwylér,* Antoine Klein, and Philippe Jetzer

Institut für Theoretische Physik, Universität Zürich, Winterthurerstrasse 190, 8057 Zürich

(Dated: August 10, 2011)

In this paper, we compute the accuracy at which the planned space-based gravitational wave detector LISA will be able to observe deviations from General Relativity. To do so, we introduce six correction parameters that account for modified gravity in the second post-Newtonian gravitational wave phase for inspiralling supermassive black hole binaries with spin precession on quasi-circular orbits. The precession of the spins and the angular momentum modulate the gravitational waveform, resulting in additional structure which could reduce correlations in the parameter space and increase the detection accuracy of the alternative theory parameters. Also, the use of higher harmonics could create further structure and increase the time during which the signal lasts in the frequency window of LISA. In order to find error distributions for the alternative theory parameters, we use the Fisher information formalism and carry out Monte Carlo simulations for 17 different binary black hole mass configurations in the range $10^5 M_\odot < M < 10^8 M_\odot$ with 10^3 randomly distributed points in the parameter space each, using the full (FWF) and restricted (RWF) version of the gravitational waveform. We find that the binaries can roughly be separated into two groups: one with low ($\lesssim 10^7 M_\odot$) and one with high total masses ($\gtrsim 10^7 M_\odot$). The RWF errors on the alternative theory parameters are two orders of magnitude higher than the FWF errors for high-mass binaries while almost comparable for low-mass binaries. Due to dilution of the available information, the accuracy of the binary parameters is reduced by factors of a few, except for the luminosity distance which is affected more seriously in the high-mass regime. As an application, we compute an optimal lower bound on the graviton mass which is increased by a factor of ~ 1.5 when using the FWF.

PACS numbers: 04.30.Db, 04.50.Kd

I. INTRODUCTION

Although General Relativity (GR) has so far passed all experimental and observational tests [1], some unsatisfactorily explained phenomena still remain which could be more elegantly described by alternative gravity theories. Among these theories are the proposed inflationary epoch of the universe shortly after the big bang which explains the temperature homogeneity of the cosmic microwave background, dark matter which should account for the missing 23% of the mass in the universe and dark energy introduced as an attempt to drive the observed late accelerated expansion of the universe. Moreover, attempts to quantize GR or to unify gravitation with the other three fundamental forces have so far all failed. Consequently, several modifications to GR have been proposed. Certain alternative theories work by introducing additional fields to the Einstein-Hilbert action of GR. Scalar-tensor field theories such as Brans-Dicke theory [2] are candidates for reproducing inflation. Modified Newtonian Dynamics (MOND) [3] attempts to get rid of dark matter by modifying the $1/r^2$ behavior of the gravitational potential; a relativistic version introducing scalar and vector fields called Tensor-Vector-Scalar gravity (TeVeS) has also been proposed [4]. The class of $f(R)$ theories [5] modify the Einstein-Hilbert action by replacing the Riemann scalar by a function of the Riemann

scalar. More phenomenological approaches such as Massive Graviton theories [6, 7] study the wave propagation of a massive gravitational field. Since alternative theories can be heavily constrained by the observation of Solar System effects and pulsar binaries [1], they are expected to reduce to GR in the limit of weak fields and to contribute significantly only in spacetime regions with strong dynamical gravity such as binary black holes (BBHs). A good review of currently discussed alternatives to GR can be found in the appendix of [8].

Among the most popular gravitational wave detectors are laser interferometers. Several ground-based interferometers such as LIGO (USA), Virgo (Italy) and GEO600 (Germany) have been built and are already operating, being sensitive to high frequencies between 10 Hz and 1 kHz. Currently LIGO is being upgraded to *Advanced LIGO* with a sensitivity ten times better, and is expected to observe several events per year and make gravitational wave detection likely within the next five years. Hence gravitational waves could finally be observed directly a hundred years after their theoretical prediction by Einstein.

Complementary to ground-based detectors restricted by their short arm-length and seismic noise at low frequencies, the spaceborne detector LISA (Laser Interferometer Space Antenna) is planned, originally as an ESA/NASA collaboration. Scheduled to be launched in the early 2020's and consisting of three spacecrafts separated by five million km in a triangular shape, LISA will form a giant laser interferometer sensitive to frequencies in the band between 10^{-5} and 1 Hz. Recently, NASA

*Electronic address: chuwylér@physik.uzh.ch

has discontinued their participation in the LISA project; the European Space Agency will try to realize the project on their own with a reduced, affordable budget [9]. The LISA science case is currently reviewed and several alternative candidates are proposed. In this paper we only discuss the originally planned LISA detector.

Among the strongest sources which LISA will detect are supermassive black hole binaries with masses between $10^5 - 10^7 M_\odot$. After a long inspiral phase, such binaries could merge into one single Kerr black hole which rings down from its excited state by emitting gravitational radiation. Compact binary inspirals produce a very clean and long-lasting gravitational signal which may be accurately described by harmonics of the orbital phase using the post-Newtonian (PN) formalism. Inspiralling BBHs emit gravitational radiation carrying information about binary parameters such as the black hole masses and the individual spins in its amplitude and phase. By using matched filtering techniques [10, 11], the binary parameters can be extracted from the noisy signal measured by the detector. Alternative gravity theories will also leave their imprints on gravitational waves, since they modify the strong-field dynamics of the BBH, resulting in a different orbital phase evolution. Also a possible graviton mass will influence gravitational waves on their way to us by making their velocity frequency dependent. Since alternative theories are heavily constrained and LISA is expected to observe signals with very high signal-to-noise ratio (SNR), a signal from a BBH will be detected with GR waveform templates regardless whether or not GR is true. This could create a fundamental bias [8] in parameter extraction if the signal is fitted with an incorrect GR waveform template, leading to incorrect parameter estimation. To fix this bias, additional parameters controlling deviations from GR can be introduced. Adding parameters while having the same information from the detectors increases the correlation between the extracted parameters and thus decreases the accuracy in the recovered parameter values.

Previous papers computed bounds which LISA could place on the Brans-Dicke parameter ω_{BD} (see e.g. [12, 13]) or on the graviton Compton wavelength λ_g (see e.g. [6]) using matched filtering. Due to the no hair theorem, for BBHs, scalar field effects in Brans-Dicke theory arising from the inner structure of compact objects cannot be distinguished; however, such massive binaries are an excellent environment to test massive graviton effects. After a first analysis of massive graviton propagation by Will [6], Berti et al. [14] introduced spin parameters and spin-orbit/spin-spin couplings, finding a loss of accuracy due to the extra parameters included in the model. Stavridis and Will [7] considered the full precession of the spins and discovered that the resulting phase modulation restores the lost accuracy on λ_g . Yagi and Tanaka [15] included eccentricity to the system and found that the additional structure through both precession and eccentricity increases the measurement accuracy by an order of magnitude. Arun and Will [16] showed that the

bounds on λ_g are improved by almost an order of magnitude for non-spinning BBHs when using the full waveform (FWF) instead of the restricted waveform (RWF) which takes the phase up to full PN order but considers the amplitude only to leading order. Taking higher harmonics into consideration increases the time during which the signal stays in the frequency window of LISA and shows a richer structure in the gravitational wave, leading to less correlation in the parameter space. Keppel and Ajith [17] used hybrid inspiral-merger-ringdown waveforms and found that they lead to a ~ 10 times higher accuracy than for inspiral-only waveforms. Moreover, Berti et al. [18] pointed out that the combination of the bounds on λ_g from individually observed inspirals in a two-year running time can again raise the accuracy by an order of magnitude. Tables summarizing lower bounds on λ_g and upper bounds on ω_{BD} found by previous works are e.g. provided by [15, 17]. Arun et al. [19] re-interpreted the matched filtering method and fitted the post-Newtonian coefficients to the waveform instead of the parameters usually extracted from them. They discussed to what extent LISA will be able to measure deviations from the 3.5PN gravitational wave phase parameters in General Relativity. Yunes and Pretorius [8] generalized this approach to a *parameterized post-Einsteinian (ppE)* framework which maps different types of alternative theories to the gravitational waveform of a compact binary merger. Cornish et al. [20] used Markov Chain Monte Carlo simulations to investigate parameter biases and possible bounds on the ppE parameters.

In this work we parameterize alternative theories by introducing corrections to the post-Newtonian coefficients of the orbital phase for a BBH inspiral, including the full 2PN precession of spins and angular momentum. We use the FWF up to 2PN instead of the RWF, summing first six harmonics. We postpone the discussion of eccentric orbits to later work and restrict our calculations to quasi-circular orbits. Since matched filtering is far more sensitive to the gravitational wave phase than to the amplitude, we do not consider corrections to the amplitude of the wave. We evaluate the measurement accuracy with which standard LISA will be able to detect such corrections for BBHs. To estimate the errors on the parameters, we make use of the Fisher information formalism which is legitimate in the limit of high SNR which LISA will provide.

The organization of this paper is as follows. In Sec. II we shortly introduce the necessary equations to describe the evolution of the inspiral phase, the spins and the angular momentum of a BBH up to 2PN. In Sec. III we introduce small departures from GR into the post-Newtonian frequency evolution equation. We then compute the modified orbital phase evolution in this scheme, incorporate it into a modified waveform template in Sec. IV, taking the waveform to be the sum of harmonics of the orbital phase, and compute the Fourier transformed waveform including alternative theory parameters. In

Sec. V we review the Fisher information formalism in order to estimate the errors on the parameters. In sec. VI we explain the details of the Monte Carlo simulations we carried out. We discuss the resulting error distributions on selected parameters in Sec. VII to see to what extent we can measure deviations from the 2PN gravitational wave phase predicted by GR and how strongly the binary parameters are affected by the introduction of six new parameters to the model. We discuss two representative BBH systems in Secs. VII A) and VII B). Because systems at higher redshifts experience higher errors, we plot the maximal redshifts for different upper error limits of the alternative theory parameters in Section VII C. As an example we calculate the resulting optimal lower bounds on the Compton wavelength of the graviton in Sec. VII D. We summarize our work and discuss possible extensions in Sec. VIII. In Appendix A we give the expressions we used for the 2.5PN and 3PN frequency evolution. We give tables with best-case, worst-case and median measurement errors of both the binary and alternative theory parameters in Appendix B.

II. EVOLUTION OF BLACK HOLE BINARIES WITH PRECESSING SPINS

A complete description of the inspiral evolution of two spinning black holes on a quasi-circular orbit with two individual masses $m_{1,2}$ and the corresponding spin vectors $\mathbf{S}_{1,2}(t)$ is given by the angular momentum unit vector $\hat{\mathbf{L}}(t)$, the orbital angular frequency $\omega(t)$ and initial values for the orbital phase $\varphi(t_0)$ and frequency $\omega(t_0)$. Further characteristics such as the orbital separation can be related to ω using post-Newtonian expressions. Therefore a quasi-circular BBH inspiral can be described by 12 intrinsic parameters. In order to relate the binary with a detector, a unit vector $\hat{\mathbf{n}}$ pointing from the detector to the barycenter, and a luminosity distance d_L between the two can be introduced, bringing an additional set of 3 extrinsic parameters into play. Thus, to describe a BBH inspiral on quasi-circular orbit, 15 parameters are required.

Since a description of the motion of such a system with full General Relativity is only possible with numerical methods and at high computational cost, an analytic expansion of the Einstein equations in powers of v/c has been studied: the post-Newtonian (PN) formalism. Currently, the equations of motion for spinning objects are known up to 2.5PN, while spin-spin and spin-orbit coupling terms are only known up to 2PN [21]. Therefore we take all the relevant expressions up to 2PN, i.e. $\mathcal{O}[(v/c)^4]$ away from leading order. The evolution equation for the angular frequency of a BBH system is [22]

$$\begin{aligned} \frac{dx}{dt} = & \frac{64\nu}{5} \frac{c^3}{GM} x^5 \left[1 - \left(\frac{743}{336} + \frac{11\nu}{4} \right) x \right. \\ & + \left(4\pi - \frac{1}{12}\beta(113, 75) \right) x^{3/2} \\ & \left. + \left(\frac{34103}{18144} + \frac{13661\nu}{2016} + \frac{59\nu^2}{18} - \frac{1}{48}\sigma(247, 721) \right) x^2 \right], \end{aligned} \quad (1)$$

where

$$x \equiv \left(\frac{GM\omega}{c^3} \right)^{2/3} \quad (2)$$

is a dimensionless orbital frequency parameter, $M = m_1 + m_2$ is the total mass and $\nu = m_1 m_2 / M^2$ is the symmetric mass ratio. The spin-orbit and spin-spin couplings are given by

$$\beta(a, b) = \frac{c}{G} \sum_{i=1}^2 \left(\frac{a}{M^2} + \frac{b\nu}{m_i^2} \right) \mathbf{S}_i \cdot \hat{\mathbf{L}}, \quad (3)$$

and

$$\sigma(a, b) = \frac{c^2}{\nu M^4 G^2} (a \mathbf{S}_1 \cdot \mathbf{S}_2 - b (\mathbf{S}_1 \cdot \hat{\mathbf{L}})(\mathbf{S}_2 \cdot \hat{\mathbf{L}})), \quad (4)$$

respectively. The precession of $\hat{\mathbf{L}}$ and $\mathbf{S}_{1,2}$ induces a time dependence for these couplings, and thus a modulation of the gravitational wave phase. Such a modulation is good for parameter estimation, since it creates extra structure which helps us decorrelate the entangled parameters. The orbit-averaged evolution equations without radiation reaction ($\dot{\mathbf{L}} + \dot{\mathbf{S}}_1 + \dot{\mathbf{S}}_2 = 0$) at leading PN order are [23]

$$\begin{aligned} \dot{\mathbf{L}} = & \frac{G}{c^2} \frac{1}{r^3} \left(\left(2 + \frac{3m_2}{2m_1} \right) \mathbf{S}_1 + \left(2 + \frac{3m_1}{2m_2} \right) \mathbf{S}_2 \right) \times \mathbf{L} \\ & - \frac{3G}{2c^2} \frac{1}{r^3} \left((\mathbf{S}_2 \cdot \hat{\mathbf{L}}) \mathbf{S}_1 + (\mathbf{S}_1 \cdot \hat{\mathbf{L}}) \mathbf{S}_2 \right) \times \hat{\mathbf{L}}, \end{aligned} \quad (5)$$

$$\dot{\mathbf{S}}_i = \frac{G}{c^2} \frac{1}{r^3} \left[\left(2 + \frac{3m_j}{2m_i} \right) \mathbf{L} + \frac{1}{2} \mathbf{S}_j - \frac{3}{2} (\mathbf{S}_j \cdot \hat{\mathbf{L}}) \hat{\mathbf{L}} \right] \times \mathbf{S}_i, \quad (6)$$

with $i \neq j$ and $i, j \in \{1, 2\}$. The orbital separation r and the angular momentum are related to the orbital frequency by the Newtonian relations

$$L = \mu \left(\frac{G^2 M^2}{\omega} \right)^{1/3}, \quad (7)$$

$$r = \left(\frac{GM}{\omega^2} \right)^{1/3}, \quad (8)$$

since higher-order corrections would exceed the 2PN order. Eqs. (1) and (7) enable us to express the evolution equations (6) in terms of the frequency ω :

$$\frac{d\mathbf{S}_i}{d\omega} = \frac{5}{96} \frac{c^3}{GM} \omega^{-2} \left[\hat{\mathbf{L}} \times \boldsymbol{\Sigma}_i + \frac{1}{2L} \left(\mathbf{S}_j - 3 \left(\mathbf{S}_j \cdot \hat{\mathbf{L}} \right) \hat{\mathbf{L}} \right) \times \mathbf{S}_i \right], \quad (9)$$

$$\begin{aligned} \frac{d\hat{\mathbf{L}}}{d\omega} &= \frac{5}{96} \frac{c^3}{GM} \omega^{-2} \frac{1}{L} \left[\boldsymbol{\Sigma}_1 + \boldsymbol{\Sigma}_2 - \frac{3}{2L} (\boldsymbol{\sigma}_1 + \boldsymbol{\sigma}_2) \right] \times \hat{\mathbf{L}} \\ &= -\frac{1}{L} \left(\frac{d\mathbf{S}_1}{d\omega} + \frac{d\mathbf{S}_2}{d\omega} \right), \end{aligned} \quad (10)$$

with

$$\boldsymbol{\Sigma}_i = \left(2 + \frac{3m_j}{2m_i} \right) \mathbf{S}_i, \quad (11)$$

and

$$\boldsymbol{\sigma}_i = \left(\mathbf{S}_j \cdot \hat{\mathbf{L}} \right) \mathbf{S}_i. \quad (12)$$

We express the gravitational wave phase in terms of the “principal + direction” [24] defined as the direction of the vector $\hat{\mathbf{L}} \times \hat{\mathbf{n}}$. A precession of the angular momentum vector changes the principal + direction. The resulting modulation of the gravitational waveform can be expressed by modifying the phase by

$$\begin{aligned} \delta\varphi &= - \int_t^{t_c} \frac{\hat{\mathbf{L}} \cdot \hat{\mathbf{n}}}{1 - (\hat{\mathbf{L}} \cdot \hat{\mathbf{n}})^2} \left(\hat{\mathbf{L}} \times \hat{\mathbf{n}} \right) \cdot \dot{\hat{\mathbf{L}}} dt \\ &= \delta\varphi_0 + \int_{\omega_0}^{\omega} \frac{\hat{\mathbf{L}} \cdot \hat{\mathbf{n}}}{1 - (\hat{\mathbf{L}} \cdot \hat{\mathbf{n}})^2} \left(\hat{\mathbf{L}} \times \hat{\mathbf{n}} \right) \cdot \frac{d\hat{\mathbf{L}}}{d\omega} d\omega, \end{aligned} \quad (13)$$

where ω_0 is the orbital frequency at time t_0 , $\delta\varphi_0 = - \int_{t_0}^{t_c} (d\delta\varphi/dt) dt$, and $d\hat{\mathbf{L}}/d\omega$ is given in Eq. (10). The resulting 2PN orbital phase is then, expressed in terms of the orbital angular frequency: $\phi(\omega) = \varphi(\omega) + \delta\varphi(\omega)$.

A signal observed from a BBH at cosmological distance is redshifted, i.e. the observed frequency is $f_o = f_e/(1+z)$, where f_e is the frequency of the gravitational waves emitted by the binary. The relation between redshift and luminosity distance in a Λ CDM cosmology without radiation and with $\Omega_\Lambda = 0.72$, $\Omega_m = 0.28$ and $H_0 = 70.1$ km/s/Mpc [25] is

$$d_L(z) = (1+z) \frac{c}{H_0} \int_0^z \frac{dz'}{\sqrt{\Omega_m(1+z')^3 + \Omega_\Lambda}}. \quad (14)$$

The previous derivations have been done for a BBH at $z = 0$. For binaries at cosmological distance, the masses are redshifted according to $\tilde{m}_{1,2} = (1+z)m_{1,2}$ and the distance between the observed system and the observer must be replaced by the luminosity distance.

Unfortunately for gravitational wave experiments, it is not possible to disentangle redshift, mass and distance: only two parameters out of these three can be inferred. Simultaneous observations of electromagnetic counterparts, through which the actual redshift could be measured, could break this correlation and lead to interesting astrophysical insights.

III. MODIFICATIONS TO THE 2PN ORBITAL PHASE

Matched filtering techniques are more sensitive to the gravitational wave phase than to the amplitude. The signal from a BBH inspiral can be described as a sum of harmonics of its orbital phase; to find the imprints of alternative gravity theories on gravitational waves it is therefore reasonable to look at how the orbital phase evolution of a BBH changes for small departures from GR. In the 2PN expansion, the orbital phase evolution can be found by integrating the frequency evolution equation (see Eq. (1) for the PN coefficients b_i)

$$\frac{dx}{dt} = \frac{64\nu}{5} \frac{c^3}{GM} x^5 \left[1 + b_1 x + b_{3/2} x^{3/2} + b_2 x^2 \right]. \quad (15)$$

As thoroughly discussed by Yunes and Pretorius in the derivation of their ppE framework [8], in the adiabatic approximation the dimensionless frequency can be expressed as

$$\frac{dx}{dt} = \frac{\dot{E}}{dE/dx}. \quad (16)$$

E is the total binding energy or Hamiltonian (conservative part) of the system while \dot{E} stands for the energy loss through gravitational waves or other physical degrees of freedom of energy loss (dissipative part). Considering the impact of alternative theories on these two quantities leads to modifications of the gravitational wave phase. Certain theories such as Brans-Dicke theory introduce scalar fields which lead to a difference in the self-gravitational binding energy \mathcal{G} per unit mass [26], producing additional dipole radiation. The energy loss formula including dipole contributions can be expressed to leading quadrupole order as [8, 26, 27]:

$$\dot{E} = -\frac{\mu^2 G^3 M^2}{c^5 r^4} \left[\frac{8}{15} (\kappa_1 v^2 - \kappa_2 \dot{r}^2) + \frac{1}{3} \kappa_D \mathcal{G}^2 \right] - \mathcal{L}_{\text{other}}. \quad (17)$$

Here, v and r are the orbital velocity and separation of the system, respectively, while κ_1 and κ_2 are so-called Peter-Mathews parameters and κ_D is a coefficient for the dipole contribution. $\mathcal{L}_{\text{other}}$ stands for any other energy loss channel, either through other polarizations or as yet unknown physical processes. Since we do not have any good parametrization for $\mathcal{L}_{\text{other}}$ so far, we do

not consider it. In terms of dimensionless frequency, the dipole radiation term in Eq. (17) leads to an additional x^{-1} term in the PN expansion (15).

We introduce a general parametrization where the effects on the phase are emphasized and no corrections to the wave amplitude are considered. The calculations are done for quasi-circular binaries with precession of both black hole spins described by the full 2PN waveform (2PN expansion of both the phase and the amplitude). We start by introducing corrections to the 2PN orbital frequency evolution dx/dt which will lead to a corrected version of the 2PN orbital phase. To do that, we introduce a correction term a_i for every 2PN coefficient b_i and an additional x^{-1} and $x^{1/2}$ term. The waveform is a series of harmonics of the orbital frequency: this results in corrections to both the amplitude and phase of the gravitational wave in frequency space. Its derivatives give the Fisher matrix elements needed for parameter estimation. Products of a correction term $a_{-1}x^{-1}$ with a PN expanded expression such as $1 + b_1x + b_{3/2}x^{3/2} + b_2x^2$ result in b_2 featuring already at 1PN order. Hence for the final result to be consistent at 2PN order, we need to do all the calculations up to 3PN, truncating at 2PN only at the very end. The current 2.5PN expansion accounts for spin-orbit effects while the 3PN expansion does not consider spin effects at all. Nevertheless, these higher order expansions can be used as approximations. The 3PN evolution equations of the dimensionless orbital angular frequency are, motivated from [22, 28] (see appendix A)

$$\left(\frac{dx}{dt}\right)_{3\text{PN}} = \frac{64\nu}{5} \frac{c^3}{GM} x^5 \left[1 + b_1x + b_{3/2}x^{3/2} + b_2x^2 + b_{5/2}x^{5/2} + b_3x^3 + b_{3,\log}x^3 \log(x) \right], \quad (18)$$

with

$$\begin{aligned} b_1 &= -\left(\frac{743}{336} + \frac{11\nu}{4}\right), \\ b_{3/2} &= \left(4\pi - \frac{1}{12}\beta(113, 75)\right), \\ b_2 &= \left(\frac{34103}{18144} + \frac{13661\nu}{2016} + \frac{59\nu^2}{18} - \frac{1}{48}\sigma(247, 721)\right), \\ b_{5/2} &= \pi\left(-\frac{4159}{672} - \frac{189\nu}{8}\right) + \frac{1}{c}\left(-\frac{40127}{1008} + \frac{1465\nu}{28}\right) \\ &\quad \times \beta(1, 0) + \frac{1}{c}\left(-\frac{583}{42} + \frac{3049\nu}{168}\right)\beta(-1, 1), \\ b_3 &= \frac{16447322263}{139708800} - \frac{1712\gamma_e}{105} + \frac{16\pi^2}{3} - \frac{56198689\nu}{217728} \\ &\quad + \frac{451\pi^2\nu}{48} + \frac{541\nu^2}{896} - \frac{5605\nu^3}{2592} - \frac{856}{105}\log(16), \\ b_{3,\log} &= -\frac{856}{105}, \end{aligned} \quad (19)$$

where β and σ are the spin-orbit and spin-spin couplings, respectively. To account for alternative theories we generalize the frequency evolution to

$$\begin{aligned} \left(\frac{dx}{dt}\right)_{\text{mod}} &= \left(\frac{dx}{dt}\right)_{3\text{PN}} + \frac{64\nu}{5} \frac{c^3}{GM} x^5 \\ &\quad \times \left[a_{-1}x^{-1} + a_0 + a_{1/2}x^{1/2} + a_1x \right. \\ &\quad \left. + a_{3/2}x^{3/2} + a_2x^2 + a_{2,\log}x^2 \log(x) \right], \end{aligned} \quad (20)$$

including corrections to every existing PN parameter and an additional x^{-1} and $x^{1/2}$ term. The reason why $x^2 \log(x)$ appears is that a term proportional to $x^3 \log(x)$ enters the 3PN phase which has to be included in 2PN corrections because of couplings with x^{-1} terms.

We now follow the steps for the derivation of the gravitational waveform presented in [29], introducing these additional corrections, keeping them at first order, and truncating at 3PN.

By inverting and integrating Eq. (20) we find the time $t(x)$ as a function of the frequency to be of the form:

$$\begin{aligned} t - t_c &\approx t(x)|_{3\text{PN}} - t_c - \frac{5}{256\nu} \frac{GM}{c^3} [T_{-1}x^{-1} + T_0 \\ &\quad + T_{1/2}x^{1/2} + T_1x + T_{3/2}x^{3/2} + T_2x^2 \\ &\quad + T_{2,\log}x^2 \log(x)]. \end{aligned} \quad (21)$$

To find the orbital phase as function of frequency, we need to recast $t(x)$ into a series expansion for $x(t)$; we are then able to find the phase by integrating $\omega \propto x^{3/2}$ over time:

$$\begin{aligned}
[\varphi(x)]_{\text{mod}} = & [\varphi(x)]_{2\text{PN}} + \frac{1}{32\nu} \frac{c^3}{GM} x^{-5/2} [A_{-1}x^{-1} \\
& + A_0 + A_{1/2}x^{1/2} + A_1x + A_{3/2}x^{3/2} \\
& + A_2x^2 + A_{2,\log}x^2 \log(x)], \quad (22)
\end{aligned}$$

with the phase corrections A_i as functions of the original orbital frequency evolution corrections a_i . At this point we choose not to consider the correction term $A_{2,\log}$ in our framework for simplicity and thus set $A_{2,\log} = 0$ in the following.

IV. MODIFICATIONS TO THE 2PN WAVEFORM

Having found a 2PN expression for the orbital phase corrections, we are able to construct the gravitational waveform as a series of harmonics of the orbital frequency:

$$h_{+, \times} = \frac{2GM\nu x}{D_L c^2} \left[\sum_{n \geq 0} \left(A_{+, \times}^{(n)} \cos(n\phi) + B_{+, \times}^{(n)} \sin(n\phi) \right) \right]. \quad (23)$$

Here, ϕ is the orbital phase of the binary with spin precession included: $\phi(t) = [\varphi(t)]_{\text{mod}} + \delta\varphi(t)$. The coefficients $A_{+, \times}^{(n)}$, $B_{+, \times}^{(n)}$ are both post-Newtonian series in x :

$$A_{+, \times}^{(n)} = \sum_{i \geq 0} a_{+, \times}^{(n, i/2)} x^{i/2}, \quad B_{+, \times}^{(n)} = \sum_{i \geq 0} b_{+, \times}^{(n, i/2)} x^{i/2}. \quad (24)$$

Explicit expressions for $A_{+, \times}^{(n)}$ and $B_{+, \times}^{(n)}$ can be found in [29]. LISA will form two different detectors with uncorrelated noise: for a detector k with antenna pattern functions F_k^+ and F_k^\times , the response function is

$$\begin{aligned}
h_k &= \frac{\sqrt{3}}{2} (F_k^+ h_+ + F_k^\times h_\times) \\
&= \frac{\sqrt{3}GM\nu x}{D_L c^2} \sum_{n \geq 0} [A_{k,n} \cos(n\psi) + B_{k,n} \sin(n\psi)], \quad (25)
\end{aligned}$$

with the antenna pattern functions

$$F_1^+(\theta_N, \phi_N, \psi_N) = \frac{1}{2} (1 + \cos^2 \theta_N) \cos 2\phi_N \cos 2\psi_N - \cos \theta_N \sin 2\phi_N \sin 2\psi_N, \quad (26)$$

$$F_1^\times(\theta_N, \phi_N, \psi_N) = F_1^+(\theta_N, \phi_N, \psi_N - \pi/4), \quad (27)$$

$$F_2^+(\theta_N, \phi_N, \psi_N) = F_1^+(\theta_N, \phi_N - \pi/4, \psi_N), \quad (28)$$

$$F_2^\times(\theta_N, \phi_N, \psi_N) = F_1^+(\theta_N, \phi_N - \pi/4, \psi_N - \pi/4). \quad (29)$$

θ_N and ϕ_N are the spherical angles of the position of the binary in the detector frame, and ψ_N is defined through

$$\tan \psi_N \equiv \frac{\hat{\mathbf{L}} \cdot \hat{\mathbf{z}} - (\hat{\mathbf{L}} \cdot \hat{\mathbf{n}})(\hat{\mathbf{z}} \cdot \hat{\mathbf{n}})}{\hat{\mathbf{n}} \cdot (\hat{\mathbf{L}} \times \hat{\mathbf{z}})}, \quad (30)$$

with $\psi = [\varphi]_{\text{mod}} + \delta\varphi + \phi_D$, including the LISA Doppler phase $\phi_D(t) = (\omega R/c) \sin \theta_N \cos(\Phi(t) - \bar{\phi}_N)$, where $R = 1$ AU and $\bar{\phi}(t) = 2\pi t/1$ yr as explained in [29]. The harmonic coefficients are

$$\begin{aligned}
A_{k,n} &= \sum_{i \geq 0} \left(F_k^+ a_+^{(n, i/2)} + F_k^\times a_\times^{(n, i/2)} \right) x^{i/2}, \\
B_{k,n} &= \sum_{i \geq 0} \left(F_k^+ b_+^{(n, i/2)} + F_k^\times b_\times^{(n, i/2)} \right) x^{i/2}. \quad (31)
\end{aligned}$$

By changing the cosine+sine representation into a cosine+phase representation, we can write Eq. (25) as

$$\begin{aligned}
h_k &= \frac{\sqrt{3}GM\nu x}{D_L c^2} \left[A_+^{(0)} F_k^+ + A_\times^{(0)} F_k^\times \right. \\
&\quad \left. + \sum_{n \geq 1} A_{k,n}^{\text{pol}} \cos(n\psi + \phi_{k,n}^{\text{pol}}) \right], \quad (32)
\end{aligned}$$

with

$$\tan \phi_{k,n}^{\text{pol}} = -\frac{B_{k,n}}{A_{k,n}}, \quad A_{k,n}^{\text{pol}} = \text{sgn}(A_{k,n}) \sqrt{A_{k,n}^2 + B_{k,n}^2}. \quad (33)$$

The Fourier transform of the response function is then, writing the cosine as an exponential and defining the new phase $\psi_{k,n} \equiv n([\varphi]_{\text{mod}} + \delta\varphi + \phi_D) + \phi_{k,n}^{\text{pol}}$:

$$\begin{aligned}
\tilde{h}_k(f) &= \frac{\sqrt{3}GM\nu}{2D_L c^2} \int_{-\infty}^{\infty} \left(\sum_{n \geq 1} x A_{k,n}^{\text{pol}} \left[e^{i(2\pi f t - \psi_{k,n})} \right. \right. \\
&\quad \left. \left. + e^{i(2\pi f t + \psi_{k,n})} \right] + 2x \left(A_+^{(0)} F_k^+ + A_\times^{(0)} F_k^\times \right) \right. \\
&\quad \left. \times e^{2\pi i f t} \right) dt. \quad (34)
\end{aligned}$$

The $n = 0$ integral accumulates around frequencies different from the gravitational wave frequency and $e^{i(2\pi f t + \psi_{k,n})}$ around negative frequencies, so both can be neglected. Then the Fourier transform reduces to

$$\tilde{h}_k(f) = \frac{\sqrt{3}GM\nu}{2D_L c^2} \sum_{n \geq 1} \left[\int_{-\infty}^{\infty} x A_{k,n}^{\text{pol}} e^{i(2\pi f t - \psi_{k,n})} dt \right]. \quad (35)$$

In the stationary phase approximation (SPA, see e.g. [30, 31]), $\tilde{h}_k(f)$ is approximated by

$$\tilde{h}_k(f) \sim \frac{\sqrt{6\pi}GM\nu}{4D_Lc^2} \sum_{n \geq 1} x(t_n) A_{k,n}^{\text{pol}}(t_n) e^{i(2\pi f t_n - \psi_{k,n} - \frac{\pi}{4})} \times \sqrt{\frac{1}{\left| \frac{d^2 \psi_{k,n}}{dt^2} \right|}}, \quad (36)$$

evaluated at the stationary points $t_n = t_{2\text{PN}}(f/n)$. The square root of the reciprocal of the second derivative of $\psi_{k,n}$ is found to be

$$\sqrt{\frac{1}{\left| \frac{d^2 \psi_{k,n}}{dt^2} \right|}} = \frac{\sqrt{5} GM}{4\sqrt{6\nu} c^3 x^{11/4}} [S(f)]_{\text{mod}}, \quad (37)$$

with $[S(f/n)]_{\text{mod}} = S_{2\text{PN}}(f/n) + \Delta S$ being a 2PN function with

$$\begin{aligned} S_{2\text{PN}}(f) &= \left[1 + \left(\frac{743}{336} + \frac{11\nu}{8} \right) x + \left(\frac{1}{24} \beta(113, 75) \right. \right. \\ &\quad \left. \left. - 2\pi \right) x^{3/2} + \left(\frac{7266251}{8128512} + \frac{18913\nu}{16128} + \frac{1379\nu^2}{1152} \right. \right. \\ &\quad \left. \left. + \frac{1}{96} \sigma(247, 721) \right) x^2 \right], \\ \Delta S &= S_{-1} x^{-1} + S_0 + S_{1/2} x^{1/2} + S_1 x + S_{3/2} x^{3/2} \\ &\quad + S_2 x^2 + S_{2,\log} x^2 \log(x). \end{aligned} \quad (38)$$

The S_i are functions of the orbital phase corrections A_i . The waveform can then be written as

$$\begin{aligned} \tilde{h}_k(f) &\sim \frac{\sqrt{5\pi\nu}G^2M^2}{8D_Lc^5} \sum_{n \geq 1} A_{k,n}^{\text{pol}}(t(f/n)) x_n^{-7/4} [S(f/n)]_{\text{mod}} \\ &\quad \times \exp \left\{ i \left[n([\Psi(f/n)]_{\text{mod}} - \delta\varphi(f/n) \right. \right. \\ &\quad \left. \left. - \phi_D[t(f/n)]) - \phi_{k,n}^{\text{pol}}[t(f/n)] \right] \right\}, \end{aligned} \quad (39)$$

where the modified phase is defined as $[\Psi(f/n)]_{\text{mod}} = [\Psi(f/n)]_{2\text{PN}} + \Delta\Psi$, with

$$\begin{aligned} \Psi_{2\text{PN}} &= \left(\frac{t_c c^3}{GM} \right) x^{3/2} - \phi_c - \frac{\pi}{4} \\ &\quad + \frac{3x^{-5/2}}{256\nu} \left[1 + \left(\frac{3715}{756} + \frac{55\nu}{9} \right) x + \left(\frac{1}{3} \beta(113, 75) \right. \right. \\ &\quad \left. \left. - 16\pi \right) x^{3/2} + \left(\frac{15293365}{508032} + \frac{27145\nu}{504} + \frac{3085\nu^2}{72} \right. \right. \\ &\quad \left. \left. + \frac{5}{24} \sigma(247, 721) \right) x^2 \right], \\ \Delta\Psi &= \frac{3}{256\nu} x^{-5/2} \left(\Psi_{-1} x^{-1} + \Psi_0 + \Psi_{1/2} x^{1/2} + \Psi_1 x \right. \\ &\quad \left. + \Psi_{3/2} x^{3/2} + \Psi_2 x^2 \right). \end{aligned} \quad (40)$$

The Ψ_i are also functions of the orbital phase corrections A_i . It makes thus sense to work only with the phase correction parameters Ψ_i from now on. The correction coefficients of ΔS are then, given as functions of Ψ_i :

$$\begin{aligned} S_{-1} &= -\frac{7}{24} \Psi_{-1}, \\ S_0 &= -\frac{35}{48} b_1 \Psi_{-1} - \frac{1}{2} \Psi_0, \\ S_{1/2} &= -\frac{49}{48} b_{3/2} \Psi_{-1} - \frac{7}{15} \Psi_{1/2}, \\ S_1 &= -\frac{21}{16} \left(\frac{b_1^2}{4} - b_2 \right) \Psi_{-1} - \frac{7}{12} b_1 \Psi_0 - \frac{3}{8} \Psi_1, \\ S_{3/2} &= \left(\frac{77}{96} b_1 b_{3/2} - \frac{49}{24} b_{5/2} \right) \Psi_{-1} - \frac{3}{4} b_{3/2} \Psi_0 \\ &\quad - \frac{7}{15} b_1 \Psi_{1/2} - \frac{1}{4} \Psi_{3/2}, \\ S_2 &= \left(-\frac{91}{384} b_1^3 + \frac{91}{96} b_1 b_2 - \frac{7}{3} b_3 + \frac{91}{192} b_{3/2}^2 \right. \\ &\quad \left. - \frac{7}{12} b_{3,\log} \right) \Psi_{-1} + \left(\frac{11}{48} b_1^2 - \frac{11}{12} b_2 \right) \\ &\quad \Psi_0 - \frac{7}{12} b_{3/2} \Psi_{1/2} - \frac{27}{80} b_1 \Psi_1 - \frac{7}{60} \Psi_2, \\ S_{2,\log} &= -\frac{7}{3} b_{3,\log} \Psi_{-1}. \end{aligned} \quad (41)$$

V. PARAMETER ESTIMATION

To estimate how accurately LISA can measure deviations from the 2PN gravitational wave phase predicted by General Relativity, we use the standard Fisher information formalism for gravitational wave experiments, as reviewed in [32, 33]. The Fisher information formalism holds only in the limit of high SNR; this is true for LISA for which SNR of a few thousands are expected. For low SNR, advanced Bayesian techniques exploring

the whole parameter space such as Markov Chain Monte Carlo methods, (see e.g. [20, 34]) are needed. Also, once data will become available, Bayesian statistics taking into account prior probability distributions will be the preferred framework.

We assume the gravitational wave signal to be buried in stationary Gaussian noise $n(t)$ such that the different Fourier components $\tilde{n}(f)$ are uncorrelated. Moreover, we presume that the noise of the two detectors is totally uncorrelated. For a signal $h(t)$ described by a true parameter set θ_t , with noise with spectral density $S_n(f)$, the probability for the measured data $d(t) = n(t) + h(t; \theta_t)$ to take this specific form is proportional to

$$p(d|\theta_t) \propto e^{-(d-h(\theta_t)|d-h(\theta_t))}, \quad (42)$$

where the inner product $(g|h)$ is defined as

$$(g|h) = 4 \operatorname{Re} \int_0^\infty \frac{\tilde{g}^*(f)\tilde{h}(f)}{S_n(f)} df. \quad (43)$$

The use of a waveform template with the parameter set θ is inaccurate by $\Delta\theta^i = \theta_t^i - \theta^i$. The errors $\Delta\theta^i$ are then approximately given by maximizing the above likelihood distribution, expanding it in the errors assumed to be small and keeping only first derivatives [33]:

$$\langle \Delta\theta_i \Delta\theta_j \rangle = \Sigma_{ij} = \Gamma_{ij}^{-1} + \mathcal{O}\left(\frac{1}{\operatorname{SNR}^4}\right), \quad (44)$$

where Σ is the covariance matrix and

$$\Gamma_{ij} = \left(\frac{\partial h}{\partial \theta^i} \middle| \frac{\partial h}{\partial \theta^j} \right) \quad (45)$$

is the so-called *Fisher matrix*. The expected measurement errors on the parameters θ^i can be expressed as

$$\Delta\theta^i = \sqrt{(\Gamma^{-1})^{ii}}. \quad (46)$$

We chose the same noise curve for standard LISA as in [29], namely the piecewise fit used by the LISA parameter estimation community [35] given by the instrumental noise

$$S_n(f) = \frac{1}{L^2} \left\{ \left[1 + \frac{1}{2} \left(\frac{f}{f_*} \right)^2 \right] S_p + \left[1 + \left(\frac{10^{-4}}{f} \right)^2 \right] \cdot \frac{4S_a}{(2\pi f)^4} \right\}, \quad (47)$$

$$(48)$$

and the confusion noise

$$S_{\text{conf}}(f) = \begin{cases} 10^{-44.62} f^{-2.3} & (f \leq 10^{-3}), \\ 10^{-50.92} f^{-4.4} & (10^{-3} < f \leq 10^{-2.7}), \\ 10^{-62.8} f^{-8.8} & (10^{-2.7} < f \leq 10^{-2.4}), \\ 10^{-89.68} f^{-20} & (10^{-2.4} < f \leq 10^{-2}), \\ 0 & (10^{-2} < f), \end{cases} \quad (49)$$

where $L = 5 \times 10^9$ m is the arm length of standard LISA, $S_p = 4 \times 10^{-22}$ m² Hz⁻¹ is the white position noise level, $S_a = 9 \times 10^{-30}$ m² s⁻⁴ Hz⁻¹ is the white acceleration noise level, and $f_* = c/(2\pi L)$ is the arm transfer frequency. The total noise curve is then $S_h(f) = S_n(f) + S_{\text{conf}}(f)$.

VI. SIMULATIONS

For our simulations 21 parameters are needed: 15 GR parameters plus 6 alternative theory parameters. We use

- (i) $\log_{10} m_1/M_\odot$ and $\log_{10} m_2/M_\odot$, for the masses of the two black holes.
- (ii) $\mu_l = \cos \theta_l$ and ϕ_l , for the spherical angles of the orbital angular momentum \mathbf{L} at $\gamma = \frac{1}{6}$.
- (iii) $\mu_1 = \cos \theta_1$ and ϕ_1 for the spherical angles of the spin of the first black hole \mathbf{S}_1 at $\gamma = \frac{1}{6}$.
- (iv) $\chi_1 = \frac{c}{Gm_1^2} |\mathbf{S}_1|$ for the dimensionless strength of the spin of the first black hole, which has to satisfy $0 \leq \chi_1 < 1$.
- (v) $\mu_2 = \cos \theta_2$, ϕ_2 , and χ_2 for the second black hole, defined equivalently as for the first one.
- (vi) t_c , the time of coalescence.
- (vii) φ_c , the phase at coalescence. As this phase is random and its determination is not of any astrophysical interest, we can safely neglect constants in the orbital phase, in particular $\delta\varphi_0$ from Eq. (13).
- (viii) $\mu_n = \cos \theta_n$ and ϕ_n , the spherical angles of the position of the binary in the sky.
- (ix) d_L , the luminosity distance between the source and the Solar System.
- (x) Ψ_i with $i \in \{-1, 0, 1/2, 1, 3/2, 2\}$, the 6 alternative theory parameters defined in section IV

All angles are taken in the frame tied to the distant stars. Moreover, we set $t = 0$ to be at the time when LISA will start operating.

We perform Monte Carlo simulations, keeping the masses $m_{1,2}$, the redshift z and the alternative theory parameters Ψ_i fixed, and randomizing all other parameters using a flat probability distribution. The spin precession equations (9) are integrated using a fourth order adaptive Runge-Kutta algorithm to find the evolution of $\hat{\mathbf{L}}(\omega)$

and $\mathbf{S}_{1,2}(\omega)$, going backwards in frequency. As a good starting point for ω we chose the frequency at the innermost circular orbit (ISCO) for a Schwarzschild black hole: $\omega_{2\text{PN}}(r_{\text{ISCO}} = 3r_s)$ where r_s is the Schwarzschild radius, as pointed out in [29]. We stop the evolution either at $t = 0$ or when the frequency of the highest harmonic goes below the LISA band ($6\omega < 3 \times 10^{-5}$ Hz). The upper and lower bounds on all the randomized parameters of the simulation are straightforward (d_L is just a function of the redshift z , defined in (14)), except for t_c for which we set a lower bound of $t_c = t_{2\text{PN}}(\omega(r = r_{\text{ISCO}}))$ using Eq. (21) and an upper bound of $t_c = 2\text{yr}$, which is the minimum science requirement for the LISA mission running time.

Using the angular momentum, spin and orbital time evolution we are able to compute the Fisher matrix (45) taking the analytical derivatives with respect to t_c , d_L , ϕ_c , μ_n , ϕ_n and all the GR correction parameters Ψ_i . The first three derivatives are easy to compute:

$$\frac{\partial \tilde{h}_k(\theta^j, f)}{\partial t_c} = 2\pi i f \tilde{h}_k(\theta^j, f), \quad (50)$$

$$\frac{\partial \tilde{h}_k(\theta^j, f)}{\partial d_L} = -\frac{\tilde{h}_k(\theta^j, f)}{d_L}, \quad (51)$$

$$\frac{\partial \tilde{h}_k(\theta^j, f)}{\partial \varphi_c} = -i \sum_n n \tilde{h}_{k,n}(\theta^j, f), \quad (52)$$

where $\tilde{h}_{k,n}$ is the n th harmonic of \tilde{h}_k . The derivatives with respect to the corrections Ψ_i are of the form

$$\begin{aligned} \frac{\partial \tilde{h}_k}{\partial \Psi_i}(f) &= \frac{\sqrt{5\pi\nu} G^2 M^2}{8D_L c^5} \sum_{n \geq 1} A_{k,n}^{\text{pol}} x_n^{-7/4} \\ &\times e^{i[n(\Psi_{\text{GR}} + \Delta\Psi - \delta\varphi - \phi_D) - \phi_{k,n}^{\text{pol}}]} \\ &\times \left(i n (S_{2\text{PN}} + \Delta S) \frac{\partial \Delta\Psi}{\partial \Psi_i} + \frac{\partial \Delta S}{\partial \Psi_i} \right), \end{aligned} \quad (53)$$

and can be calculated in a straightforward way. The derivatives which we could not compute analytically are approximated by

$$\frac{\partial \tilde{h}_k(\theta^j, f)}{\partial \theta^i} \approx \frac{\tilde{h}_k(\theta^j + \epsilon \delta^{ij}/2, f) - \tilde{h}_k(\theta^j - \epsilon \delta^{ij}/2, f)}{\epsilon}, \quad (54)$$

where ϵ is a small displacement of the parameter θ_i which we chose to be of the constant value $\epsilon = 10^{-7}$ for every parameter, except for ϕ_l for which ϵ was divided by $2 - 2|\mu_l|$, μ_i ($i \in \{1, 2\}$) for which ϵ was divided by $5\chi_i$, and ϕ_i for which ϵ was divided by $10\chi_i(1 - |\mu_i|)$. The formula is accurate up to $O(\epsilon^2)$.

For each set of parameters we then compute the Fisher matrix using *Clenshaw-Curtis quadrature* and then invert it in order to find the corresponding errors on the parameters which we analyze in section VII. In order to

avoid matrix inversion problems, we use a normalization of the Fisher-Matrix so that all diagonal elements are $A_{ii} = 1$ and all off-diagonal elements are in the range $A_{ij} \in [-1; 1]$:

$$A_{ij} \equiv \frac{1}{\sqrt{\Gamma_{ii}\Gamma_{jj}}} \Gamma_{ij}. \quad (55)$$

After inversion, the covariance matrix can then be recovered with

$$\Sigma_{ij} = \frac{1}{\sqrt{\Gamma_{ii}\Gamma_{jj}}} A_{ij}^{-1}. \quad (56)$$

In situations where $\hat{\mathbf{L}} \cdot \hat{\mathbf{n}}$ is close to 1, the Runge Kutta method fails to converge because

$$\frac{d\delta\varphi}{d\omega} = \frac{\hat{\mathbf{L}} \cdot \hat{\mathbf{n}}}{1 - (\hat{\mathbf{L}} \cdot \hat{\mathbf{n}})^2} (\hat{\mathbf{L}} \times \hat{\mathbf{n}}) \cdot \frac{d\hat{\mathbf{L}}}{d\omega} \xrightarrow{\hat{\mathbf{L}} \cdot \hat{\mathbf{n}} \rightarrow 1} \infty. \quad (57)$$

Whenever this happens, we take the approximate value

$$\begin{aligned} \delta\varphi(\omega + \delta\omega) &\approx \\ \delta\varphi(\omega) + \text{angle} \left[\left(\hat{\mathbf{L}}(\omega + \delta\omega) \times \hat{\mathbf{n}} \right), \left(\hat{\mathbf{L}}(\omega) \times \hat{\mathbf{n}} \right) \right], \end{aligned} \quad (58)$$

as explained in [29].

VII. RESULTS

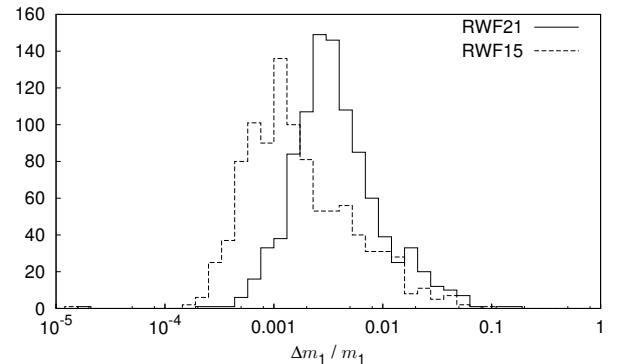


FIG. 1: Comparison between the estimated distributions of the measurement error on m_1 for a low-mass binary system $m_1 = 1 \times 10^6 M_\odot$ and $m_2 = 3 \times 10^5 M_\odot$ with (RWF21) and without (RWF15) including alternative theory parameters, using only the restricted waveform.

We performed simulations for 17 different mass configurations, with total masses between $10^5 M_\odot$ and $10^8 M_\odot$,

mass ratios varying between 1:1 and 1:10, and using 10^3 points in the parameter space for each configuration.

The redshift has been kept fixed to $z = 1$ since it is not possible to disentangle redshift, mass and distance. The signal coming from a binary with masses $m_{1,2}$ at redshift z and luminosity distance $d_L(z)$ can be expressed with one from an apparent binary with $\tilde{m}_{1,2} = \frac{1+z}{1+z_0} m_{1,2}$ at redshift z_0 and luminosity distance $d_L(z_0)$ multiplied by an overall factor of $d_L(z_0)/d_L(z)$. Thus every BBH inspiral producing a signal at redshift z can be described with a waveform template at redshift z_0 . The Fisher matrix scales as

$$\begin{aligned}\Gamma_{ij}^{(z)} &= \left(\frac{\partial h}{\partial \theta^i}(m_1, m_2, z) \middle| \frac{\partial h}{\partial \theta^j}(m_1, m_2, z) \right) \\ &= \left(\frac{d_L(z_0)}{d_L(z)} \right)^2 \left(\frac{\partial h}{\partial \theta^i}(\tilde{m}_1, \tilde{m}_2, z_0) \middle| \frac{\partial h}{\partial \theta^j}(\tilde{m}_1, \tilde{m}_2, z_0) \right) \\ &= \left(\frac{d_L(z_0)}{d_L(z)} \right)^2 \Gamma_{ij}^{(z_0)}.\end{aligned}\quad (59)$$

The errors on the parameters scale then with

$$\Delta\theta^i(z) = \frac{d_L(z)}{d_L(z_0)} \Delta\theta^i(z_0). \quad (60)$$

Since we choose to work in a picture where General Relativity is the theory assumed to be true and we are keen to know how well LISA will be able to measure deviations from its post-Newtonian expansion terms ψ_i , we fixed the alternative theory parameters to the fiducial values $\Psi_i = 0$.

For each of the 17 binaries we computed the best-case measurement error (5% quantile), the typical error (median) and the worst-case error (95% quantile) for the

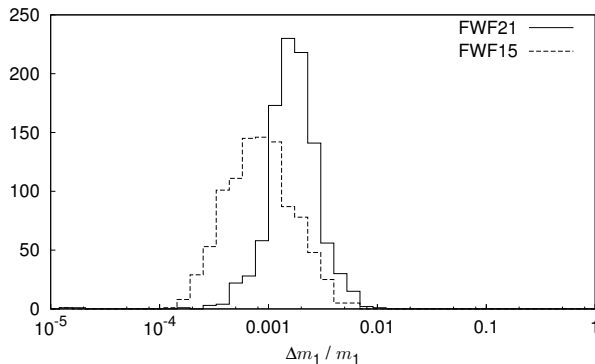


FIG. 2: Comparison between the estimated distributions of the measurement error on m_1 for a low-mass binary system $m_1 = 1 \times 10^6 M_\odot$ and $m_2 = 3 \times 10^5 M_\odot$ with (FWF21) and without (FWF15) including alternative theory parameters and using the full waveform.

full (FWF) and restricted waveforms (RWF) and present them in tables I-XIV. For each BBH parameter we are interested in, we give an error table with (21 parameters in total) and without (15 parameters in total) including the alternative theory parameters Ψ_i . We do this to show how much accuracy is lost by introducing alternative theory corrections into a GR waveform template. For binaries where no signal can be extracted from the dataset, we fix the error to infinity.

We give the errors on the sky localization not in terms of errors on μ_n and ϕ_n but instead in terms of an error ellipse with principal axes $2a$ and $2b$, enclosing the region outside of which there is an $1/e$ probability of finding the binary, following [36].

Moreover, in tables XV-XX we give measurement errors on the alternative theory parameters, using both the RWF and FWF.

We roughly divide the binaries into two classes: low-mass binaries ($M \lesssim 10^7 M_\odot$) and high-mass binaries ($M \gtrsim 10^7 M_\odot$). Below we discuss these two cases, using BBHs with $m_1 = 10^6 M_\odot$, $m_2 = 3 \times 10^5 M_\odot$ and $m_1 = 3 \times 10^7 M_\odot$, $m_2 = 10^7 M_\odot$ as representative examples for low-mass and high-mass binaries respectively. We find when using both the RWF and the FWF, the error distributions of the mass and spin parameters behave similarly, losing a factor 1.2 – 5 of accuracy when alternative theory parameters are included. The error on the orientation of the binary $2a$ and $2b$ is at maximum an order of magnitude worse. For high-mass binaries, factors of ~ 10 and ~ 100 are lost in the determination of the luminosity distance d_L , using the FWF and RWF respectively. While the RWF/FWF errors on the alternative theory parameters are almost equal for low-mass binaries, the RWF errors are about 100 times higher for high-mass binaries

A. Low-mass binaries

For low-mass binaries with total masses below $10^7 M_\odot$ we find that in general, using the FWF instead of the RWF improves the measurement errors $\Delta\Psi_i$ on the alternative theory parameters by a factor of $\sim 1.5 - 3$. The correlation with the new parameters causes a decrease in the accuracy of the 15 existing parameters. For both the FWF and the RWF, the errors on the mass and spin parameters m_1 , m_2 , χ_1 and χ_2 are typically worse by a factor of 2 – 5 while the luminosity distance d_L is approximately half as accurate. The angular orientation errors $2a$ and $2b$ increase only by $\sim 10\%$; this is reasonable, since we do not expect alternative theories to correlate strongly with rotations on a large scale. Therefore it is not necessary to use the FWF instead of the RWF for the sole purpose of measuring alternative gravity parameters in the low-mass regime.

We present selected distributions of the measurement errors $\Delta m_1/m_1$, $\Delta\chi_1/\chi_1$, $2a$, $\Delta d_L/d_L$ and all the six $\Delta\Psi_i$ in figures 1-14. The error distributions of $\Delta m_2/m_2$,

$\Delta\chi_2/\chi_2$ and $2b$ are similar to the ones of $\Delta m_1/m_1$, $\Delta\chi_1/\chi_1$ and $2a$.

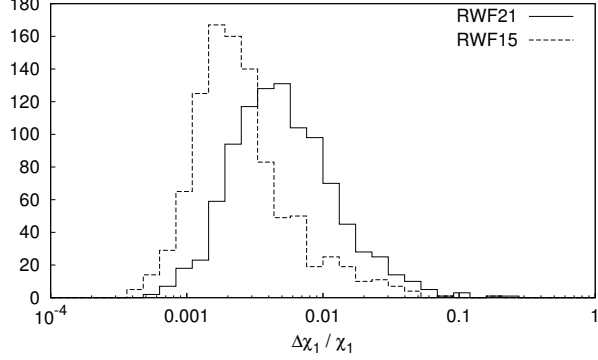


FIG. 3: Comparison between the estimated distributions of the measurement error on χ_1 for a low-mass binary system $m_1 = 1 \times 10^6 M_\odot$ and $m_2 = 3 \times 10^5 M_\odot$ with (RWF21) and without (RWF15) including alternative theory parameters, using only the restricted waveform.

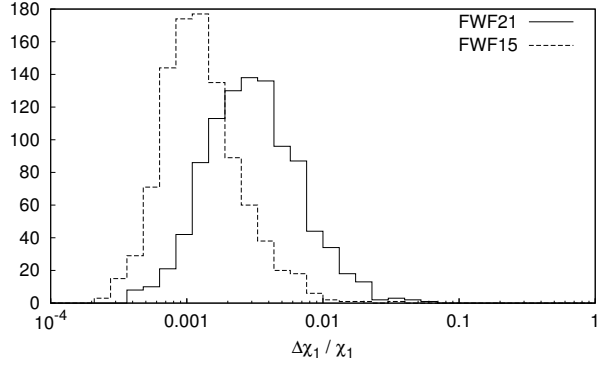


FIG. 4: Comparison between the estimated distributions of the measurement error on χ_1 for a low-mass binary system $m_1 = 1 \times 10^6 M_\odot$ and $m_2 = 3 \times 10^5 M_\odot$ with (FWF21) and without (FWF15) including alternative theory parameters and using the full waveform.

B. High-mass binaries

By using the FWF instead of the RWF for high-mass binaries with total masses $\gtrsim 10^7 M_\odot$, we find significant improvements for the measurement errors of the alternative theory parameters by factors of $\sim 100 - 1000$ for $\Delta\Psi_{-1}$, $\sim 30 - 60$ for $\Delta\Psi_0$ and $\Delta\Psi_{1/2}$, and $\sim 10 - 100$ for $\Delta\Psi_1$, $\Delta\Psi_{3/2}$ and $\Delta\Psi_2$. This makes it clear that it is inevitable to use the FWF in the high-mass regime. In any case, since the second harmonic spends only a few orbits in the LISA band, the use of the RWF is not trustworthy. Moreover, for BBHs with total masses higher than $10^8 M_\odot$, LISA will not be able to see the second harmonic

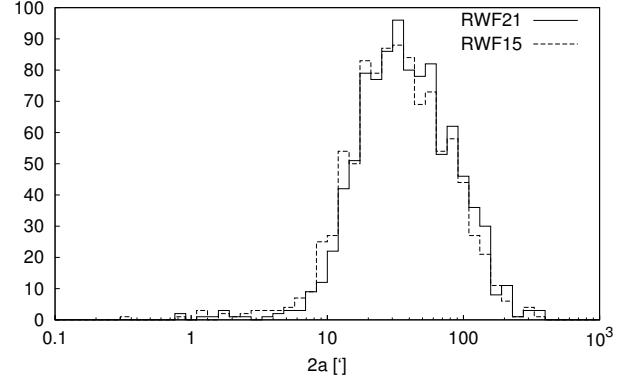


FIG. 5: Comparison between the estimated distributions of the major axis of the positioning error ellipse for a low-mass binary system $m_1 = 1 \times 10^6 M_\odot$ and $m_2 = 3 \times 10^5 M_\odot$ with (RWF21) and without (RWF15) including alternative theory parameters, using only the restricted waveform.

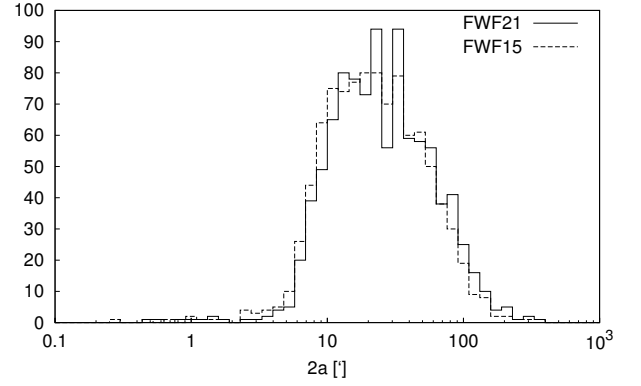


FIG. 6: Comparison between the estimated distributions of the major axis of the positioning error ellipse for a low-mass binary system $m_1 = 1 \times 10^6 M_\odot$ and $m_2 = 3 \times 10^5 M_\odot$ with (FWF21) and without (FWF15) including alternative theory parameters and using the full waveform.

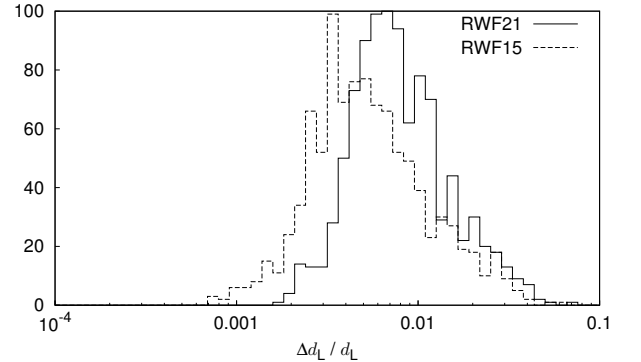


FIG. 7: Comparison between the estimated distributions of the measurement error on d_L for a low-mass binary system $m_1 = 1 \times 10^6 M_\odot$ and $m_2 = 3 \times 10^5 M_\odot$ with (RWF21) and without (RWF15) including alternative theory parameters, using only the restricted waveform.

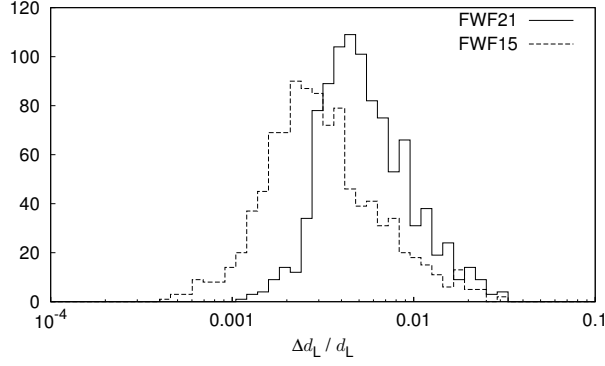


FIG. 8: Comparison between the estimated distributions of the measurement error on d_L for a low-mass binary system $m_1 = 1 \times 10^6 M_\odot$ and $m_2 = 3 \times 10^5 M_\odot$ with (FWF21) and without (FWF15) including alternative theory parameters, using only the restricted waveform.

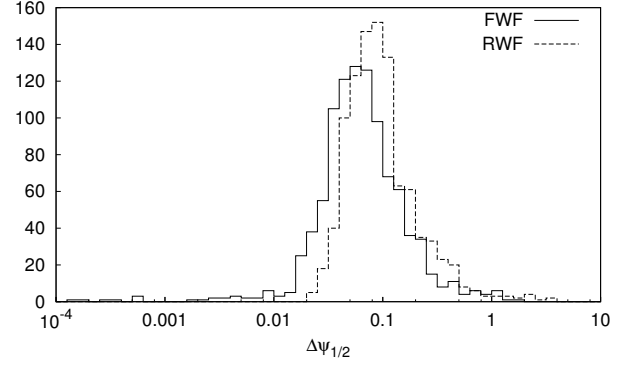


FIG. 11: Comparison between the estimated distributions of the measurement error on the alternative theory parameter $\Psi_{1/2}$ for a low-mass binary system $m_1 = 1 \times 10^6 M_\odot$ and $m_2 = 3 \times 10^5 M_\odot$, using the RWF and the FWF.

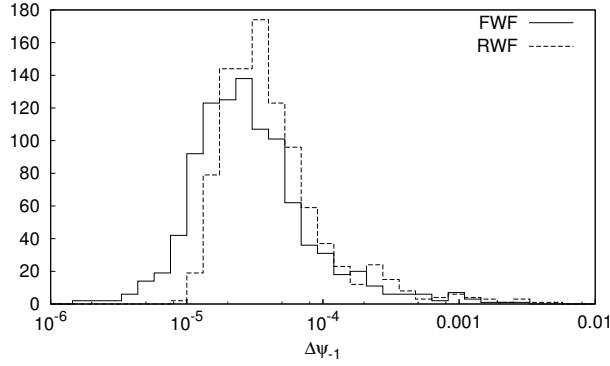


FIG. 9: Comparison between the estimated distributions of the measurement error on the alternative theory parameter Ψ_{-1} for a low-mass binary system $m_1 = 1 \times 10^6 M_\odot$ and $m_2 = 3 \times 10^5 M_\odot$, using the restricted waveform (RWF) and the full waveform (FWF).

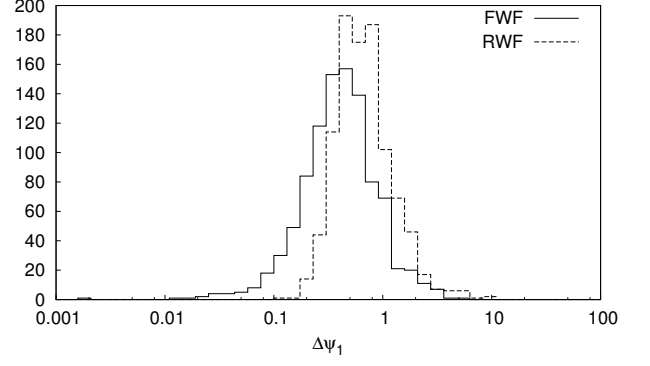


FIG. 12: Comparison between the estimated distributions of the measurement error on the alternative theory parameter Ψ_1 for a low-mass binary system $m_1 = 1 \times 10^6 M_\odot$ and $m_2 = 3 \times 10^5 M_\odot$, using the RWF and the FWF.

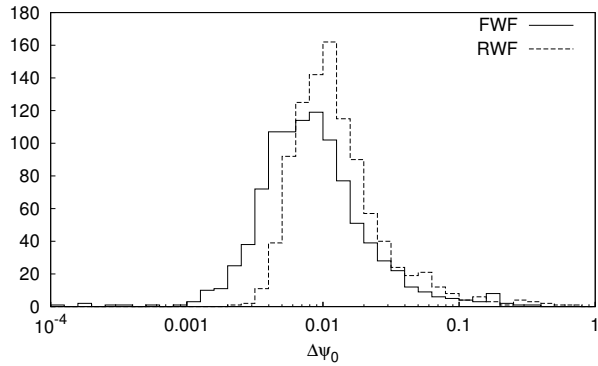


FIG. 10: Comparison between the estimated distributions of the measurement error on the alternative theory parameter Ψ_0 for a low-mass binary system $m_1 = 1 \times 10^6 M_\odot$ and $m_2 = 3 \times 10^5 M_\odot$, using the RWF and the FWF.

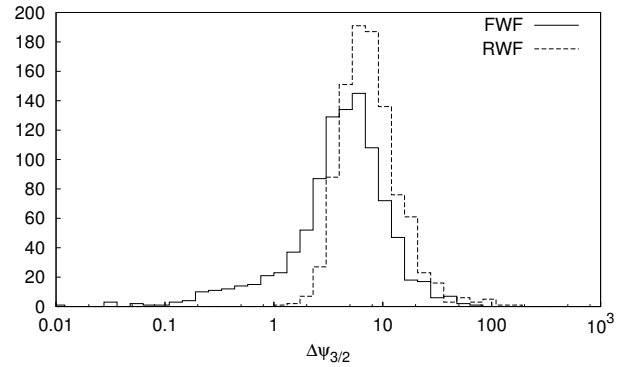


FIG. 13: Comparison between the estimated distributions of the measurement error on the alternative theory parameter $\Psi_{3/2}$ for a low-mass binary system $m_1 = 1 \times 10^6 M_\odot$ and $m_2 = 3 \times 10^5 M_\odot$, using the RWF and the FWF.

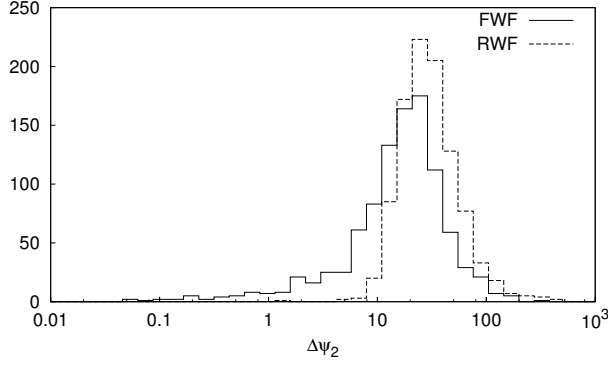


FIG. 14: Comparison between the estimated distributions of the measurement error on the alternative theory parameter Ψ_2 for a low-mass binary system $m_1 = 1 \times 10^6 M_\odot$ and $m_2 = 3 \times 10^5 M_\odot$, using the RWF and the FWF.

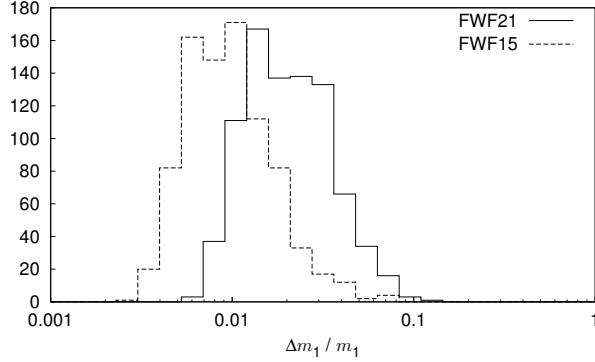


FIG. 15: Comparison between the estimated distributions of the measurement error on m_1 for a high-mass binary system $m_1 = 3 \times 10^7 M_\odot$ and $m_2 = 1 \times 10^7 M_\odot$ with (FWF21) and without (FWF15) including alternative theory parameters and using the full waveform.

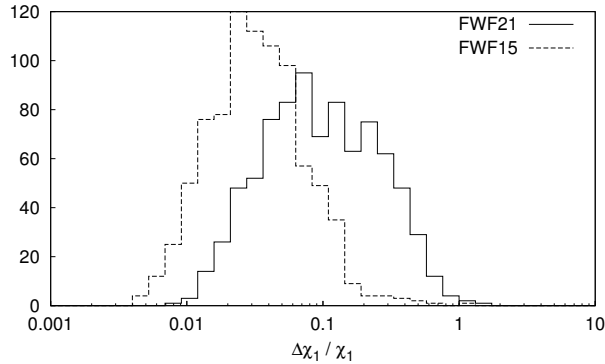


FIG. 16: Comparison between the estimated distributions of the measurement error on χ_1 for a high-mass binary system $m_1 = 3 \times 10^7 M_\odot$ and $m_2 = 1 \times 10^7 M_\odot$ with (FWF21) and without (FWF15) including alternative theory parameters and using the full waveform.

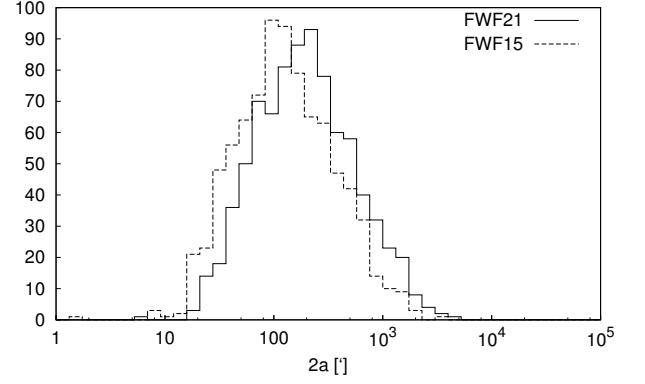


FIG. 17: Comparison between the estimated distributions of the major axis of the positioning error ellipse for a high-mass binary system $m_1 = 3 \times 10^7 M_\odot$ and $m_2 = 1 \times 10^7 M_\odot$ with (FWF21) and without (FWF15) including alternative theory parameters and using the full waveform.

at all and so the RWF cannot be used. For both the FWF and the RWF, the errors on the mass and spin parameters m_1 , m_2 , χ_1 and χ_2 are typically worse by a factor of $\sim 1.2 - 4$ when accounting for alternative gravity parameters. The luminosity distance d_L is about 50 – 1000 times less accurate for the RWF while for the FWF it is only $\sim 10 - 100$ times worse. For the FWF, the angular orientation error $2a$ and $2b$ is at maximum 5 times worse while the RWF loses up to a factor of ~ 10 in accuracy.

We present selected distributions of the measurement errors $\Delta m_1 / m_1$, $\Delta \chi_1 / \chi_1$, $2a$, $\Delta d_L / d_L$ and all the six $\Delta \Psi_i$ in figures 15-24.

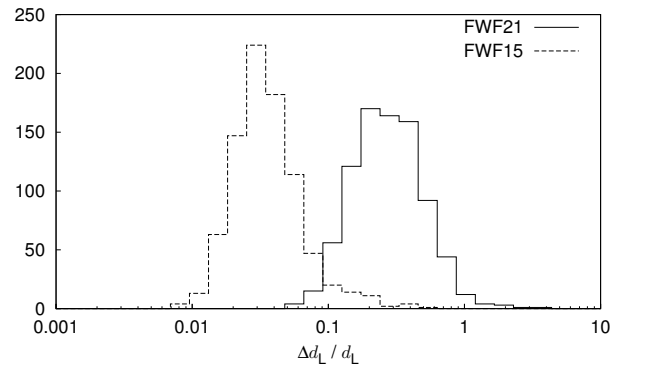


FIG. 18: Comparison between the estimated distributions of the measurement error on d_L for a high-mass binary system $m_1 = 3 \times 10^7 M_\odot$ and $m_2 = 1 \times 10^7 M_\odot$ with (FWF21) and without (FWF15) including alternative theory parameters, using only the restricted waveform.

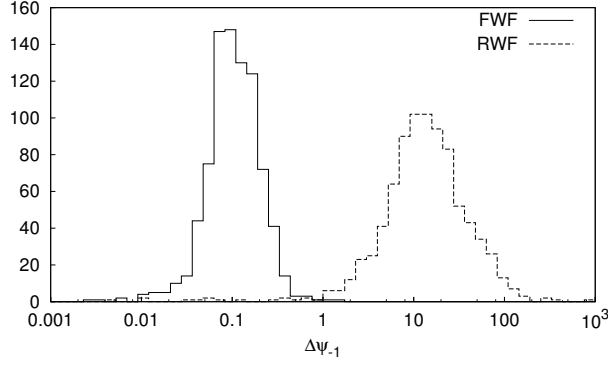


FIG. 19: Comparison between the estimated distributions of the measurement error on the alternative theory parameter Ψ_{-1} for a high-mass binary system $m_1 = 3 \times 10^7 M_\odot$ and $m_2 = 1 \times 10^7 M_\odot$, using the RWF and the FWF.

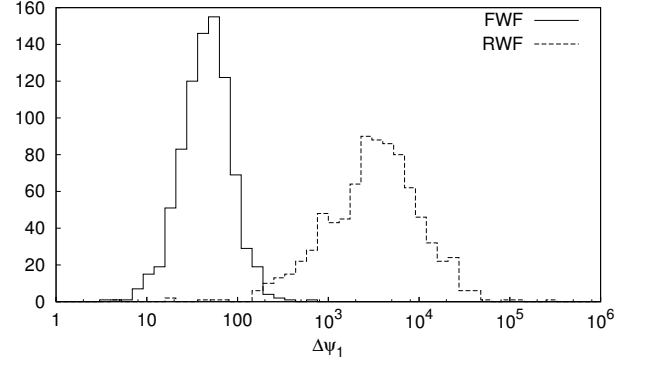


FIG. 22: Comparison between the estimated distributions of the measurement error on the alternative theory parameter Ψ_1 for a high-mass binary system $m_1 = 3 \times 10^7 M_\odot$ and $m_2 = 1 \times 10^7 M_\odot$, using the RWF and the FWF.

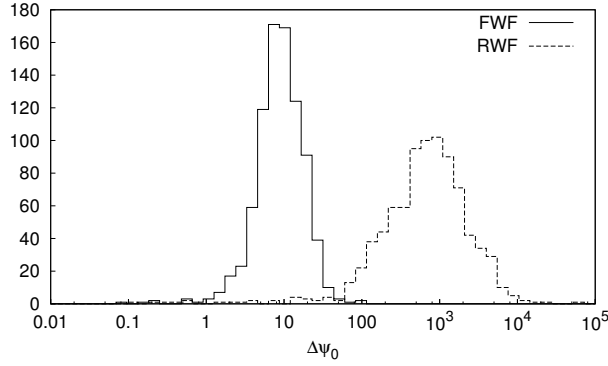


FIG. 20: Comparison between the estimated distributions of the measurement error on the alternative theory parameter Ψ_0 for a high-mass binary system $m_1 = 3 \times 10^7 M_\odot$ and $m_2 = 1 \times 10^7 M_\odot$, using the RWF and the FWF.

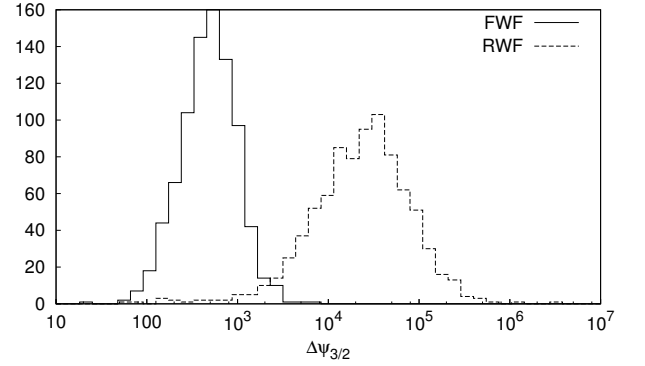


FIG. 23: Comparison between the estimated distributions of the measurement error on the alternative theory parameter $\Psi_{3/2}$ for a high-mass binary system $m_1 = 3 \times 10^7 M_\odot$ and $m_2 = 1 \times 10^7 M_\odot$, using the RWF and the FWF.

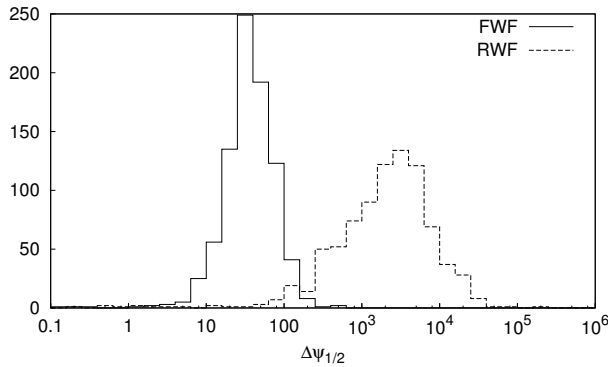


FIG. 21: Comparison between the estimated distributions of the measurement error on the alternative theory parameter $\Psi_{1/2}$ for a high-mass binary system $m_1 = 3 \times 10^7 M_\odot$ and $m_2 = 1 \times 10^7 M_\odot$, using the RWF and the FWF.

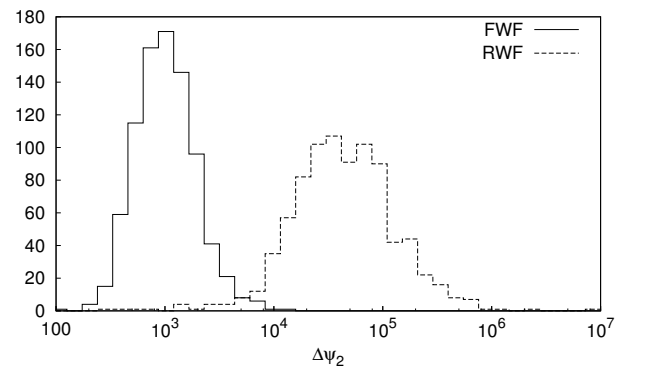


FIG. 24: Comparison between the estimated distributions of the measurement error on the alternative theory parameter Ψ_2 for a high-mass binary system $m_1 = 3 \times 10^7 M_\odot$ and $m_2 = 1 \times 10^7 M_\odot$, using the RWF and the FWF.

C. Upper limits for redshifted masses

All the errors tabularized in appendix B are given for the fixed redshift $z = 1$. Some of them in the high-mass regime are apparently too high at $z = 1$. Nevertheless, since the measurement accuracy of the parameters is correlated with the redshift as given in Eq. (60), for an equivalent mass configuration at a lower redshift the errors should reduce to reasonable values. Since we do not know the actual values of the alternative theory parameters, we cannot fix the accuracy with which we want to measure $\Psi_i(z)$. For this reason, we introduce the relative accuracy parameter α such that $|\Delta\Psi_i(z)/\psi_i| < \alpha$ where ψ_i is the fiducial 2PN phase coefficient from $\Psi_{2\text{PN}}$ in Eq. (40). The maximal redshift is then given as

$$z_{\text{max}} = z \left(\alpha d_L(z_0) |\Delta\Psi_i(z_0)/\psi_i|^{-1} \right), \quad (61)$$

where $z(d_L)$ is the inverse of (14) and can be computed numerically. We use here the 5%-quantile for $\Delta\Psi_i(z_0 = 1)$ as given in the tables in appendix B, i.e. we define the (optimistic) maximal redshift as the redshift where 5% of the binaries in the sample can still be seen with relative accuracy less than α . Since we expect corrections to the 2PN phase parameters of GR to be small (at least for the lower PN orders), we focus here on a relative accuracy below 10%. At redshift $z = 1$ this accuracy is already difficult to reach for binaries with masses above $10^6 M_\odot$ (see also [19]). It is important to emphasize that we concentrate here on actually measuring the alternative theory parameters instead of just set-

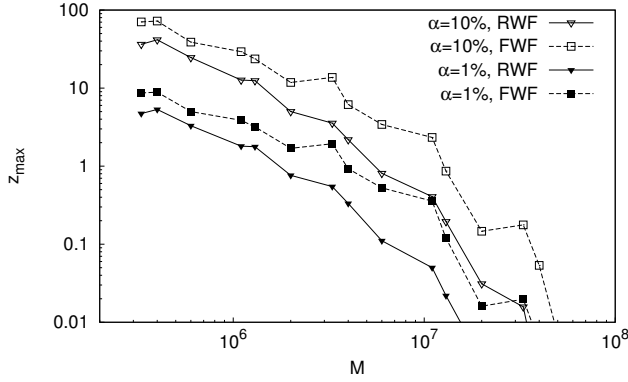


FIG. 25: Maximal redshifts for the alternative theory parameter Ψ_0 such that the relative error $\Delta\Psi_0/\psi_0$ is smaller than α . ψ_0 is the corresponding fiducial 2PN phase coefficient. For a relative error of 1%, low-mass binaries are suitable up to redshifts $z \sim 1 - 10$ while high-mass binaries can be observed up to $z \sim 0.01 - 0.1$.

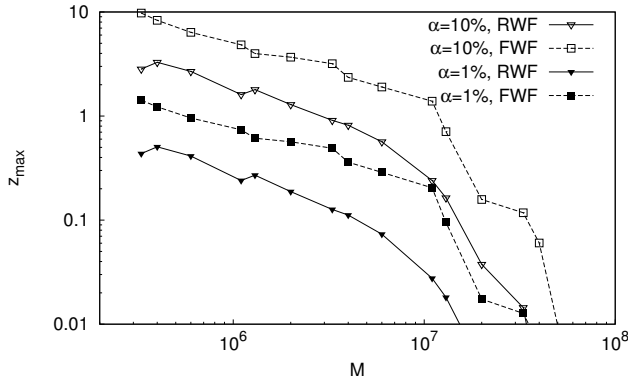


FIG. 26: Maximal redshifts for the alternative theory parameter Ψ_1 such that the relative error $\Delta\Psi_1/\psi_1$ is smaller than α . ψ_1 is the corresponding fiducial 2PN phase coefficient. For a relative error of 1%, low-mass binaries are suitable up to redshifts $z \sim 0.1 - 1$ while high-mass binaries can be observed up to $z \sim 0.01 - 0.1$.

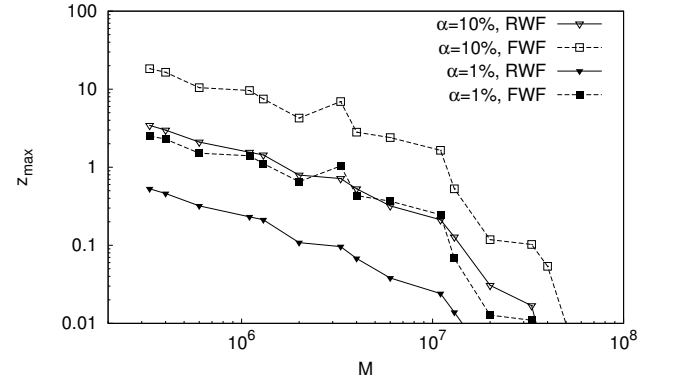


FIG. 27: Maximal redshifts for the alternative theory parameter $\Psi_{3/2}$ such that the relative error $\Delta\Psi_{3/2}/\psi_{3/2}$ is smaller than α . $\psi_{3/2}$ is the corresponding fiducial 2PN phase coefficient. For a relative error of 1%, low-mass binaries are suitable up to redshifts $z \sim 0.1 - 1$ while high-mass binaries can be observed up to $z \sim 0.01 - 0.1$.

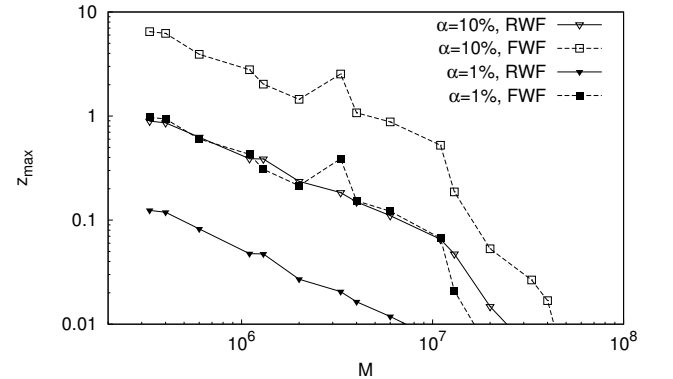


FIG. 28: Maximal redshifts for the alternative theory parameter Ψ_2 such that the relative error $\Delta\Psi_2/\psi_2$ is smaller than α . ψ_2 is the corresponding fiducial 2PN phase coefficient. For a relative error of 1%, low-mass binaries are suitable up to redshifts $z \sim 0.1 - 1$ while high-mass binaries can be observed up to $z \sim 0.01 - 0.1$.

ting bounds upon them. In figures 25-28 we present the maximal redshifts at which LISA can still measure the alternative theory parameters Ψ_0 , Ψ_1 , $\Psi_{3/2}$ and Ψ_2 for certain mass configurations with relative accuracies of $\alpha = 10\%$ and $\alpha = 1\%$. Since for Ψ_{-1} and $\Psi_{1/2}$ the fiducial 2PN phase coefficients are zero, we do not consider them. We checked that the error roughly scales with the redshift. For a relative accuracy of 1%, Ψ_0 is measurable up to redshifts of $z \sim 1 - 10$ for low-mass binaries and up to redshifts of $z \sim 0.01 - 0.1$ for high-mass binaries. Ψ_1 , $\Psi_{3/2}$ and Ψ_2 can all be detected with a relative accuracy of 1% up to redshifts of $z \sim 0.1 - 1$ for low masses and $z \sim 0.01 - 0.1$ for high masses. For Ψ_0 , the use of the FWF improves the maximal redshifts by about a factor of 2 for low masses and up to a factor of 10 for high masses, while the maximal redshifts are improved by almost an order of magnitude for the rest of the alternative theory parameters. If we were lucky and LISA could find a low-mass black hole binary at very low redshift $z = 0.1$, we would be able to recover the alternative theory parameters with ~ 10 times smaller errors than given in tables XV-XX.

D. Example: Lower bound on graviton mass

In order to compare our results with previous work in the field, we present here a lower bound on the graviton mass from our results at redshift $z = 1$. According to [6], the effect of a massive graviton can be accounted for by introducing a gravitational wave phase correction

$$\Delta\Psi_{\text{MG}} = -\beta \nu^{-3/5} x^{-3/2}, \quad (62)$$

where x is the dimensionless frequency, ν is the symmetric mass ratio and the parameter β is defined as

$$\beta = \frac{G \pi^2 D(z) \mathcal{M}}{c^2 \lambda_g^2 (1+z)}. \quad (63)$$

Here λ_g is the Compton wavelength of the graviton, z is the redshift, $\mathcal{M} = (1+z)M\nu^{3/5}$ is the *measured* chirp mass affected by redshift, and $D(z)$ is the distance given as

$$D(z) = (1+z) \frac{c}{H_0} \int_0^z \frac{dz'}{(1+z')^2 \sqrt{\Omega_M(1+z')^3 + \Omega_\Lambda}}, \quad (64)$$

where H_0 , Ω_M and Ω_Λ are defined as in section II. In our framework, this is similar to the correction in Eq. (40):

$$\Delta\Psi_{\text{MG}} = \frac{3}{256\nu} x^{-3/2} \Psi_1. \quad (65)$$

Hence the errors on β and Ψ_1 can be related with

$$\Delta\beta = \frac{3}{256} \nu^{-2/5} \Delta\Psi_1. \quad (66)$$

We take the fiducial value $\beta = 0$, thus the error $\Delta\beta$ sets an upper bound on possible values for β . A lower bound on the Compton wavelength of the graviton can then be calculated as

$$\lambda_g > \sqrt{\frac{256 G \pi^2 D(z) M \nu}{3 c^2 (1+z) \Delta\Psi_1}}, \quad (67)$$

where M is the redshifted total mass of the binary. We find that optimal lower bounds on λ_g originate from a $(3 \times 10^6 + 1 \times 10^7) M_\odot$ binary for the FWF and from a $(1 \times 10^6 + 1 \times 10^6) M_\odot$ binary for the RWF. Including all six alternative theory parameters Ψ_i , the resulting average bounds are $\lambda_g > 1.2 \times 10^{21}$ cm (FWF) and $\lambda_g > 7.8 \times 10^{20}$ cm (RWF). These bounds are both lower than the one Yagi and Tanaka [15] found ($\lambda_g > 3.1 \times 10^{21}$ cm) using the RWF and simple precession at a distance of 3 Gpc; this is because the presence of the other five alternative theory parameters increases correlations among the parameters. If we consider only one correction parameter Ψ_1 which among other things accounts for massive gravity, the bounds increase to $\lambda_g > 7.6 \times 10^{21}$ cm (FWF) and $\lambda_g > 4.9 \times 10^{21}$ cm (RWF). The RWF bound is slightly higher than the one by Yagi and Tanaka for a $(10^6 + 10^7) M_\odot$ binary; for this mass configuration we found a lower RWF bound of $\lambda_g > 2.8 \times 10^{21}$ cm. Cornish et al. [20] found a similar optimal RWF bound of $\lambda_g > 3.8 \times 10^{21}$ cm. The use of the FWF improves the bound on the graviton Compton wavelength by a factor of ~ 1.5 with respect to the RWF, regardless whether only one or all the alternative theory parameters are included into the simulations.

VIII. CONCLUSION AND OUTLOOK

We analyzed the expected measurement error distributions of 17 different mass configurations of supermassive black hole binaries with masses between $10^5 - 10^8 M_\odot$. We found that the black hole binaries can roughly be divided into two groups: low-mass binaries with $M \lesssim 10^7 M_\odot$ and high-mass binaries with $M \gtrsim 10^7 M_\odot$. Comparing the results of the simulations using the FWF and the RWF, we found that the RWF errors on the alternative theory parameters Ψ_i are a factor of ~ 100 times higher than the FWF errors for high-mass binaries, while they are almost comparable for low-mass binaries. Due to the dilution of the available information through the introduction of six extra parameters, the original parameters lose accuracy. For masses and spins this is only a factor of 1.2-5 for both low- and high-mass binaries regardless of whether the FWF or RWF is used. The loss of accuracy on the position of the black hole binary on

the sky is at maximum 10% for low-mass binaries and up to a factor of 5 for high-mass binaries. However, the accuracy of the luminosity distance is affected more seriously for high-mass binaries, using the RWF results in a loss of a factor of $\sim 50 - 1000$ while using the FWF reduces it to factors of $\sim 10 - 100$. For low-mass binaries it is only about a factor of 2 worse. The use of the FWF is therefore mandatory for high-mass binaries, while the parameter estimation is more efficient for low-mass binaries and only up to a factor of 5 times worse when the RWF is used instead of the FWF.

Since the error distributions were all calculated at fixed redshift $z = 1$ but the errors increase with redshift, we computed typical maximal redshifts up to which the alternative theory parameters are detectable with a relative accuracy smaller than 1% for the best 5% of the binaries in the sample. We found that for a deviation of 1% from the fiducial value, Ψ_0 is detectable up to redshifts of $z \sim 1 - 10$ for low total masses and up to $z \sim 0.01 - 0.1$ for high total masses. The rest of the alternative theory parameters Ψ_1 , $\Psi_{3/2}$ and Ψ_2 with a fiducial 2PN phase coefficient unequal zero are detectable up to redshifts of $z \sim 0.1 - 1$ for low-mass binaries and $z \sim 0.01 - 0.1$ for high-mass binaries with the same relative accuracy. The use of the FWF improves the maximal redshifts up to a factor of 10 for high total masses.

The FWF enables us to increase the optimal lower bound on the Compton wavelength of the graviton by about a factor of 1.5 compared to the one reached by the RWF. We achieve an optimal lower bound of $\lambda_g > 7.6 \times 10^{21}$ cm if only the alternative theory parameter Ψ_1 is considered.

Since ESA is now considering a reduced LISA mission, certain aspects of the mission have to be reassessed. Several reduced variants of LISA are currently reviewed and will have an effect on the measurement accuracy of the mission [18]. It is thus of great importance to use as accurate waveform templates as possible to restore the lost accuracy with computational power on Earth. The use of the FWF improves the accuracy of the alternative theory parameters by at least an order of magnitude compared to the RWF. As shown by [16], the use of hybrid inspiral-merger-ringdown templates instead of inspiral-only templates improves the accuracy by an order of magnitude for the RWF; it would be interesting to find out how much such templates are improved when the FWF is used. The accuracy can further be enhanced by about an order of magnitude when considering combined observations instead of just extracting alternative theory parameters from individual black hole binaries [18]. Also effects of eccentric orbits should be accounted for to make the model more realistic.

Future work could include the introduction of amplitude corrections such as in [8], since certain alternative theories are only visible in the gravitational wave amplitude (e.g. Chern-Simons-modified gravity [37]). Also, the underlying mechanism of spin precession should be analyzed for effects originating from possible alternative

theories. In this paper we neglected the energy loss of black hole binaries through unexpected physical effects such as further degrees of freedom in the propagation of gravitational waves arising from additional polarizations (e.g. longitudinal modes). It would be interesting to create a parameterized model for these effects. Also, since we studied a search for modifications at different PN orders at the same time, one could use the results of this work to investigate how the use of next-to-leading order modifications of GR could affect the determination of alternative theory parameters.

Acknowledgments

C. H. would like to thank Sylvain Marsat for interesting discussions about the post-Newtonian expansion. C. H. and A. K. are supported by the Swiss National Science Foundation.

Appendix A: The 2.5PN and 3PN orbital frequency evolution equations

The inclusion of dipole radiation corrections proportional to x^{-1} requires the knowledge of higher PN orders to be consistent to 2PN order, namely 2.5PN and 3PN contributions. Since the current 2.5PN expansion just considers spin-orbit contributions and no spin-spin effects, and the 3PN expansion does not account for any spin coupling effects at all, these are of course only approximations.

1. 2.5PN from Blanchet et al. 2006

Blanchet et al. 2006 [22] compute the angular frequency evolution for a binary with symmetric mass ratio ν as

$$\begin{aligned} \frac{\dot{\omega}}{\omega^2} = & \frac{96}{5} \nu x^{5/2} \left\{ 1 + x \left(-\frac{743}{336} - \frac{11}{4} \nu \right) + 4\pi x^{3/2} \right. \\ & + x^2 \left(\frac{34103}{18144} + \frac{13661}{2016} \nu + \frac{59}{18} \nu^2 \right) + \\ & \pi x^{5/2} \left(-\frac{4159}{672} - \frac{189}{8} \nu \right) + \frac{x^{3/2}}{Gm^2} \left[-\frac{47}{3} S_l \right. \\ & \left. - \frac{25}{4} \frac{\delta m}{m} \Sigma_l \right] + \frac{x^{5/2}}{Gm^2} \left[\left(-\frac{40127}{1008} + \frac{1465}{28} \nu \right) S_l \right. \\ & \left. + \left(-\frac{583}{42} + \frac{3049}{168} \nu \right) \frac{\delta m}{m} \Sigma_l \right] + O\left(\frac{1}{c^6}\right), \end{aligned} \quad (\text{A1})$$

where $\omega = c^3/(GM) x^{3/2}$, $\delta m = m_1 - m_2$ is the mass difference and $m = m_1 + m_2$ is the total mass. The spin interaction terms are expressed with

$$\boldsymbol{\Sigma} = m \left[\frac{\mathbf{S}_2}{m_2} - \frac{\mathbf{S}_1}{m_1} \right], \quad S_l = \mathbf{S} \cdot \mathbf{l}, \quad \Sigma_l = \boldsymbol{\Sigma} \cdot \mathbf{l}, \quad (\text{A2})$$

where $\mathbf{S} = \mathbf{S}_1 + \mathbf{S}_2$ is the total spin and $\mathbf{l} = \frac{\mathbf{L}}{|\mathbf{L}|}$ is the angular momentum unit vector. This enables us to write Eq. (A1) in the same form as Eq. (18), and we recover

$$b_{5/2} = \pi \left(-\frac{4159}{672} - \frac{189}{8} \nu \right) + \frac{1}{Gm^2} \left[\left(-\frac{40127}{1008} + \frac{1465}{28} \nu \right) S_l + \left(-\frac{583}{42} + \frac{3049}{168} \nu \right) \frac{\delta m}{m} \Sigma_l \right]. (\text{A3})$$

2. 3PN without spin terms from Blanchet et al. 2002

In Luc Blanchet's living review [21] (see also [38–40]), the 3PN expression for the total energy of non-spinning compact binaries can be found to be

$$E = -\frac{1}{2} \mu c^2 x \left\{ 1 + \left(-\frac{3}{4} - \frac{1}{12} \nu \right) x + \left(-\frac{27}{8} + \frac{19}{8} \nu - \frac{1}{24} \nu^2 \right) x^2 + \left(-\frac{675}{64} + \left[\frac{34445}{576} - \frac{205}{96} \pi^2 \right] \nu - \frac{155}{96} \nu^2 - \frac{35}{5184} \nu^3 \right) x^3 \right\}, \quad (\text{A4})$$

and the energy flux is

$$\begin{aligned} \frac{dE}{dt} = & -\frac{32c^5}{5G} \nu^2 x^5 \left\{ 1 + \left(-\frac{1247}{336} - \frac{35}{12} \nu \right) x + 4\pi x^{3/2} \right. \\ & + \left(-\frac{44711}{9072} + \frac{9271}{504} \nu + \frac{65}{18} \nu^2 \right) x^2 + \left(-\frac{8191}{672} - \frac{535}{24} \nu \right) \pi x^{5/2} \\ & + \left(\frac{6643739519}{69854400} + \frac{16}{3} \pi^2 - \frac{1712}{105} C - \frac{856}{105} \log(16x) + \left[-\frac{134543}{7776} + \frac{41}{48} \pi^2 \right] \nu - \frac{94403}{3024} \nu^2 - \frac{775}{324} \nu^3 \right) x^3 \\ & \left. + \left(-\frac{16285}{504} + \frac{176419}{1512} \nu + \frac{19897}{378} \nu^2 \right) \times \pi x^{7/2} \right\}. \end{aligned} \quad (\text{A5})$$

Here ν is the symmetric mass ratio and $C = 0.577..$ is the Euler constant. The logarithm in dE/dt will lead to a logarithmic term in the 3PN expansion. The PN coefficients b_i can be recovered by computing the frequency evolution as a series in the dimensionless frequency x in the adiabatic approximation:

$$\begin{aligned} \frac{dx}{dt} &= \frac{dE}{dt} \left(\frac{dE}{dx} \right)^{-1} \\ &= \frac{64\nu}{5} \frac{c^3}{Gm} x^5 \left[b_1 x + b_{3/2} x^{3/2} + b_2 x^2 + b^{5/2} x^{5/2} + b_3 x^3 + b_{3,\log} x^3 \log(x) \right], \end{aligned} \quad (\text{A6})$$

with

$$\begin{aligned} b_3 &= \frac{16447322263}{139708800} - \frac{1712\gamma_e}{105} + \frac{16\pi^2}{3} - \frac{56198689\nu}{217728} \\ &+ \frac{451\pi^2\nu}{48} + \frac{541\nu^2}{896} - \frac{5605\nu^3}{2592} - \frac{856}{105} \log(16), \\ b_{3,\log} &= -\frac{856}{105}. \end{aligned} \quad (\text{A7})$$

Appendix B: Tables

TABLE I: Median, 5% and 95% quantiles of the estimated measurement errors on m_1 for different mass configurations at redshift $z = 1$ with alternative theory parameters included.

$m_1[M_\odot]$	$m_2[M_\odot]$	$\Delta m_1/m_1$ with corrections					
		5%-quantile		Median		95%-quantile	
		RWF	FWF	RWF	FWF	RWF	FWF
3×10^5	3×10^4	5.8×10^{-4}	4.2×10^{-4}	1.6×10^{-3}	1.1×10^{-3}	7.4×10^{-3}	2.8×10^{-3}
3×10^5	1×10^5	4.6×10^{-4}	3.8×10^{-4}	1.7×10^{-3}	8.9×10^{-4}	1.0×10^{-2}	2.2×10^{-3}
3×10^5	3×10^5	6.1×10^{-4}	3.8×10^{-4}	2.5×10^{-3}	1.0×10^{-3}	1.7×10^{-2}	2.7×10^{-3}
1×10^6	1×10^5	1.2×10^{-3}	8.4×10^{-4}	2.8×10^{-3}	1.8×10^{-3}	1.3×10^{-2}	4.5×10^{-3}
1×10^6	3×10^5	9.6×10^{-4}	6.8×10^{-4}	3.4×10^{-3}	1.7×10^{-3}	2.2×10^{-2}	3.9×10^{-3}
1×10^6	1×10^6	1.2×10^{-3}	8.4×10^{-4}	5.4×10^{-3}	2.5×10^{-3}	4.5×10^{-2}	6.5×10^{-3}
3×10^6	3×10^5	2.2×10^{-3}	1.2×10^{-3}	6.1×10^{-3}	2.7×10^{-3}	3.2×10^{-2}	6.3×10^{-3}
3×10^6	1×10^6	2.5×10^{-3}	1.3×10^{-3}	1.1×10^{-2}	2.8×10^{-3}	5.4×10^{-2}	7.3×10^{-3}
3×10^6	3×10^6	4.8×10^{-3}	2.4×10^{-3}	3.0×10^{-2}	9.4×10^{-3}	0.26	2.7×10^{-2}
1×10^7	1×10^6	1.1×10^{-2}	2.1×10^{-3}	3.9×10^{-2}	4.0×10^{-3}	0.13	8.6×10^{-3}
1×10^7	3×10^6	1.8×10^{-2}	2.0×10^{-3}	9.4×10^{-2}	5.0×10^{-3}	0.32	1.4×10^{-2}
1×10^7	1×10^7	0.15	1.7×10^{-2}	0.76	3.3×10^{-2}	4.2	7.1×10^{-2}
3×10^7	3×10^6	0.13	5.7×10^{-3}	0.39	1.2×10^{-2}	1.0	2.4×10^{-2}
3×10^7	1×10^7	0.39	9.2×10^{-3}	1.1	2.0×10^{-2}	3.4	5.0×10^{-2}
3×10^7	3×10^7	3.8	6.1×10^{-2}	30	0.15	390	0.5
1×10^8	1×10^7	∞	0.13	∞	0.34	∞	1.6
1×10^8	3×10^7	∞	1.3	∞	4.2	∞	53

TABLE II: Median, 5% and 95% quantiles of the estimated measurement errors on m_1 for different mass configurations at redshift $z = 1$ without considering alternative theory parameters.

$m_1[M_\odot]$	$m_2[M_\odot]$	$\Delta m_1/m_1$ without corrections					
		5%-quantile		Median		95%-quantile	
		RWF	FWF	RWF	FWF	RWF	FWF
3×10^5	3×10^4	1.1×10^{-4}	8.4×10^{-5}	3.3×10^{-4}	2.4×10^{-4}	3.5×10^{-3}	3.5×10^{-3}
3×10^5	1×10^5	1.8×10^{-4}	1.4×10^{-4}	8.2×10^{-4}	4.8×10^{-4}	7.8×10^{-3}	7.8×10^{-3}
3×10^5	3×10^5	1.8×10^{-4}	1.3×10^{-4}	1.2×10^{-3}	2.8×10^{-4}	9.0×10^{-3}	9.0×10^{-3}
1×10^6	1×10^5	2.5×10^{-4}	1.5×10^{-4}	7.0×10^{-4}	4.4×10^{-4}	5.2×10^{-3}	5.2×10^{-3}
1×10^6	3×10^5	3.7×10^{-4}	2.6×10^{-4}	1.4×10^{-3}	8.1×10^{-4}	1.4×10^{-2}	1.4×10^{-2}
1×10^6	1×10^6	3.5×10^{-4}	2.6×10^{-4}	2.3×10^{-3}	6.8×10^{-4}	2.1×10^{-2}	2.1×10^{-2}
3×10^6	3×10^5	3.8×10^{-4}	2.1×10^{-4}	1.2×10^{-3}	6.5×10^{-4}	1.3×10^{-2}	1.3×10^{-2}
3×10^6	1×10^6	8.5×10^{-4}	4.8×10^{-4}	3.6×10^{-3}	1.1×10^{-3}	3.1×10^{-2}	3.1×10^{-2}
3×10^6	3×10^6	1.1×10^{-3}	3.7×10^{-4}	8.1×10^{-3}	8.1×10^{-4}	9.7×10^{-2}	9.7×10^{-2}
1×10^7	1×10^6	1.1×10^{-3}	4.0×10^{-4}	4.0×10^{-3}	1.3×10^{-3}	4.7×10^{-2}	4.7×10^{-2}
1×10^7	3×10^6	2.9×10^{-3}	7.8×10^{-4}	1.6×10^{-2}	1.8×10^{-3}	0.15	0.15
1×10^7	1×10^7	2.1×10^{-2}	2.1×10^{-3}	0.18	5.6×10^{-3}	1.6	1.6
3×10^7	3×10^6	1.5×10^{-2}	1.7×10^{-3}	9.8×10^{-2}	5.1×10^{-3}	0.58	0.58
3×10^7	1×10^7	0.33	4.5×10^{-3}	0.96	9.3×10^{-3}	2.9	2.9
3×10^7	3×10^7	3.5	5.4×10^{-2}	21	0.13	240	240
1×10^8	1×10^7	∞	9.8×10^{-2}	∞	0.25	∞	∞
1×10^8	3×10^7	∞	0.87	∞	3.1	∞	∞

TABLE III: Median, 5% and 95% quantiles of the estimated measurement errors on m_2 for different mass configurations at redshift $z = 1$ with alternative theory parameters included.

$m_1[M_\odot]$	$m_2[M_\odot]$	$\Delta m_2/m_2$ with corrections					
		5%-quantile		Median		95%-quantile	
		RWF	FWF	RWF	FWF	RWF	FWF
3×10^5	3×10^4	1.6×10^{-4}	1.2×10^{-4}	6.3×10^{-4}	4.5×10^{-4}	5.8×10^{-3}	2.5×10^{-3}
3×10^5	1×10^5	3.2×10^{-4}	2.3×10^{-4}	1.2×10^{-3}	7.9×10^{-4}	9.1×10^{-3}	2.2×10^{-3}
3×10^5	3×10^5	5.9×10^{-4}	4.0×10^{-4}	2.7×10^{-3}	1.0×10^{-3}	1.8×10^{-2}	2.8×10^{-3}
1×10^6	1×10^5	3.5×10^{-4}	2.5×10^{-4}	1.3×10^{-3}	8.5×10^{-4}	1.1×10^{-2}	4.4×10^{-3}
1×10^6	3×10^5	6.6×10^{-4}	4.9×10^{-4}	2.3×10^{-3}	1.5×10^{-3}	1.9×10^{-2}	4.2×10^{-3}
1×10^6	1×10^6	1.2×10^{-3}	8.7×10^{-4}	5.6×10^{-3}	2.5×10^{-3}	4.4×10^{-2}	6.4×10^{-3}
3×10^6	3×10^5	6.8×10^{-4}	3.8×10^{-4}	2.5×10^{-3}	1.4×10^{-3}	2.8×10^{-2}	7.5×10^{-3}
3×10^6	1×10^6	1.6×10^{-3}	7.9×10^{-4}	6.1×10^{-3}	2.9×10^{-3}	3.9×10^{-2}	1.0×10^{-2}
3×10^6	3×10^6	4.6×10^{-3}	2.3×10^{-3}	3.2×10^{-2}	9.4×10^{-3}	0.26	2.7×10^{-2}
1×10^7	1×10^6	2.8×10^{-3}	1.0×10^{-3}	1.4×10^{-2}	4.0×10^{-3}	0.12	1.7×10^{-2}
1×10^7	3×10^6	5.5×10^{-3}	1.6×10^{-3}	2.9×10^{-2}	6.5×10^{-3}	0.25	2.3×10^{-2}
1×10^7	1×10^7	0.17	1.7×10^{-2}	0.78	3.3×10^{-2}	4.2	7.1×10^{-2}
3×10^7	3×10^6	8.1×10^{-2}	5.9×10^{-3}	0.39	1.9×10^{-2}	2.4	7.3×10^{-2}
3×10^7	1×10^7	1.2	1.5×10^{-2}	4.2	3.4×10^{-2}	21	0.11
3×10^7	3×10^7	3.4	6.0×10^{-2}	32	0.15	360	0.5
1×10^8	1×10^7	∞	0.91	∞	2.6	∞	11
1×10^8	3×10^7	∞	5.0	∞	20	∞	290

TABLE IV: Median, 5% and 95% quantiles of the estimated measurement errors on m_2 for different mass configurations at redshift $z = 1$ without considering alternative theory parameters.

$m_1[M_\odot]$	$m_2[M_\odot]$	$\Delta m_2/m_2$ without corrections					
		5%-quantile		Median		95%-quantile	
		RWF	FWF	RWF	FWF	RWF	FWF
3×10^5	3×10^4	7.9×10^{-5}	6.0×10^{-5}	2.4×10^{-4}	1.7×10^{-4}	2.5×10^{-3}	2.5×10^{-3}
3×10^5	1×10^5	1.5×10^{-4}	1.2×10^{-4}	6.7×10^{-4}	3.9×10^{-4}	6.3×10^{-3}	6.3×10^{-3}
3×10^5	3×10^5	1.8×10^{-4}	1.3×10^{-4}	1.2×10^{-3}	2.8×10^{-4}	9.0×10^{-3}	9.0×10^{-3}
1×10^6	1×10^5	1.7×10^{-4}	1.1×10^{-4}	5.0×10^{-4}	3.1×10^{-4}	3.7×10^{-3}	3.7×10^{-3}
1×10^6	3×10^5	3.0×10^{-4}	2.1×10^{-4}	1.1×10^{-3}	6.5×10^{-4}	1.1×10^{-2}	1.1×10^{-2}
1×10^6	1×10^6	3.6×10^{-4}	2.6×10^{-4}	2.2×10^{-3}	6.7×10^{-4}	2.1×10^{-2}	2.1×10^{-2}
3×10^6	3×10^5	2.9×10^{-4}	1.6×10^{-4}	8.6×10^{-4}	4.6×10^{-4}	8.9×10^{-3}	8.9×10^{-3}
3×10^6	1×10^6	7.0×10^{-4}	4.0×10^{-4}	2.9×10^{-3}	9.2×10^{-4}	2.5×10^{-2}	2.5×10^{-2}
3×10^6	3×10^6	1.2×10^{-3}	3.6×10^{-4}	8.3×10^{-3}	8.1×10^{-4}	9.8×10^{-2}	9.8×10^{-2}
1×10^7	1×10^6	1.1×10^{-3}	3.9×10^{-4}	3.2×10^{-3}	9.8×10^{-4}	3.3×10^{-2}	3.3×10^{-2}
1×10^7	3×10^6	2.8×10^{-3}	7.2×10^{-4}	1.3×10^{-2}	1.5×10^{-3}	0.12	0.12
1×10^7	1×10^7	2.3×10^{-2}	2.1×10^{-3}	0.17	5.6×10^{-3}	1.7	1.7
3×10^7	3×10^6	3.8×10^{-2}	2.6×10^{-3}	0.13	5.2×10^{-3}	0.56	0.56
3×10^7	1×10^7	0.41	5.8×10^{-3}	1.4	1.3×10^{-2}	4.9	4.9
3×10^7	3×10^7	3.1	5.4×10^{-2}	21	0.13	250	250
1×10^8	1×10^7	∞	0.34	∞	1.0	∞	∞
1×10^8	3×10^7	∞	3.0	∞	11	∞	∞

TABLE V: Median, 5% and 95% quantiles of the estimated measurement errors on χ_1 for different mass configurations at redshift $z = 1$ with alternative theory parameters included.

$m_1[M_\odot]$	$m_2[M_\odot]$	$\Delta \chi_1$ with corrections					
		5%-quantile		Median		95%-quantile	
		RWF	FWF	RWF	FWF	RWF	FWF
3×10^5	3×10^4	3.3×10^{-4}	2.3×10^{-4}	1.1×10^{-3}	7.1×10^{-4}	4.8×10^{-3}	2.8×10^{-3}
3×10^5	1×10^5	8.8×10^{-4}	6.0×10^{-4}	3.1×10^{-3}	2.1×10^{-3}	1.5×10^{-2}	1.0×10^{-2}
3×10^5	3×10^5	1.9×10^{-3}	1.5×10^{-3}	1.4×10^{-2}	9.3×10^{-3}	0.24	0.12
1×10^6	1×10^5	6.8×10^{-4}	4.3×10^{-4}	2.0×10^{-3}	1.2×10^{-3}	7.7×10^{-3}	4.0×10^{-3}
1×10^6	3×10^5	1.4×10^{-3}	9.2×10^{-4}	4.7×10^{-3}	3.0×10^{-3}	2.6×10^{-2}	1.2×10^{-2}
1×10^6	1×10^6	3.3×10^{-3}	2.4×10^{-3}	2.8×10^{-2}	1.7×10^{-2}	0.58	0.22
3×10^6	3×10^5	1.3×10^{-3}	6.9×10^{-4}	3.7×10^{-3}	1.9×10^{-3}	1.6×10^{-2}	6.6×10^{-3}
3×10^6	1×10^6	3.0×10^{-3}	1.4×10^{-3}	1.3×10^{-2}	4.9×10^{-3}	6.2×10^{-2}	2.4×10^{-2}
3×10^6	3×10^6	1.7×10^{-2}	7.9×10^{-3}	0.17	5.4×10^{-2}	2.4	0.58
1×10^7	1×10^6	5.3×10^{-3}	1.5×10^{-3}	1.8×10^{-2}	4.3×10^{-3}	7.4×10^{-2}	1.4×10^{-2}
1×10^7	3×10^6	1.1×10^{-2}	2.3×10^{-3}	6.2×10^{-2}	9.1×10^{-3}	0.33	5.1×10^{-2}
1×10^7	1×10^7	0.62	8.3×10^{-2}	4.1	0.45	26	3.5
3×10^7	3×10^6	0.1	6.6×10^{-3}	0.41	2.2×10^{-2}	2.1	7.3×10^{-2}
3×10^7	1×10^7	1.4	2.1×10^{-2}	4.4	9.0×10^{-2}	16	0.45
3×10^7	3×10^7	14	3.1	81	13	1.5×10^3	85
1×10^8	1×10^7	∞	0.76	∞	2.7	∞	10
1×10^8	3×10^7	∞	8.8	∞	28	∞	270

TABLE VI: Median, 5% and 95% quantiles of the estimated measurement errors on χ_1 for different mass configurations at redshift $z = 1$ without considering alternative theory parameters.

$m_1[M_\odot]$	$m_2[M_\odot]$	$\Delta\chi_1$ without corrections					
		5%-quantile		Median		95%-quantile	
		RWF	FWF	RWF	FWF	RWF	FWF
3×10^5	3×10^4	1.9×10^{-4}	1.2×10^{-4}	4.3×10^{-4}	2.6×10^{-4}	2.2×10^{-3}	2.2×10^{-3}
3×10^5	1×10^5	4.9×10^{-4}	3.0×10^{-4}	1.5×10^{-3}	8.4×10^{-4}	8.3×10^{-3}	8.3×10^{-3}
3×10^5	3×10^5	1.0×10^{-3}	7.9×10^{-4}	6.2×10^{-3}	3.6×10^{-3}	8.4×10^{-2}	8.4×10^{-2}
1×10^6	1×10^5	3.7×10^{-4}	1.9×10^{-4}	9.0×10^{-4}	4.6×10^{-4}	2.6×10^{-3}	2.6×10^{-3}
1×10^6	3×10^5	8.5×10^{-4}	5.0×10^{-4}	2.2×10^{-3}	1.2×10^{-3}	1.4×10^{-2}	1.4×10^{-2}
1×10^6	1×10^6	1.6×10^{-3}	1.2×10^{-3}	1.1×10^{-2}	6.0×10^{-3}	0.17	0.17
3×10^6	3×10^5	4.7×10^{-4}	2.2×10^{-4}	1.2×10^{-3}	5.7×10^{-4}	5.5×10^{-3}	5.5×10^{-3}
3×10^6	1×10^6	1.2×10^{-3}	6.2×10^{-4}	3.7×10^{-3}	1.6×10^{-3}	2.8×10^{-2}	2.8×10^{-2}
3×10^6	3×10^6	4.2×10^{-3}	2.6×10^{-3}	4.1×10^{-2}	1.5×10^{-2}	0.68	0.68
1×10^7	1×10^6	1.4×10^{-3}	4.5×10^{-4}	3.4×10^{-3}	1.0×10^{-3}	1.6×10^{-2}	1.6×10^{-2}
1×10^7	3×10^6	3.6×10^{-3}	1.1×10^{-3}	1.5×10^{-2}	3.0×10^{-3}	0.1	0.1
1×10^7	1×10^7	0.13	2.1×10^{-2}	1.1	0.13	9.7	9.7
3×10^7	3×10^6	3.8×10^{-2}	2.7×10^{-3}	0.15	6.8×10^{-3}	0.69	0.69
3×10^7	1×10^7	0.45	9.2×10^{-3}	1.8	3.2×10^{-2}	6.7	6.7
3×10^7	3×10^7	13	1.1	75	5.1	1.0×10^3	1.0×10^3
1×10^8	1×10^7	∞	0.25	∞	1.3	∞	∞
1×10^8	3×10^7	∞	4.3	∞	16	∞	∞

TABLE VII: Median, 5% and 95% quantiles of the estimated measurement errors on χ_2 for different mass configurations at redshift $z = 1$ with alternative theory parameters included.

$m_1[M_\odot]$	$m_2[M_\odot]$	$\Delta\chi_2$ with corrections					
		5%-quantile		Median		95%-quantile	
		RWF	FWF	RWF	FWF	RWF	FWF
3×10^5	3×10^4	2.0×10^{-3}	1.2×10^{-3}	1.5×10^{-2}	1.0×10^{-2}	0.16	8.9×10^{-2}
3×10^5	1×10^5	1.7×10^{-3}	1.1×10^{-3}	1.0×10^{-2}	6.9×10^{-3}	8.4×10^{-2}	4.8×10^{-2}
3×10^5	3×10^5	2.0×10^{-3}	1.5×10^{-3}	1.4×10^{-2}	9.0×10^{-3}	0.23	0.13
1×10^6	1×10^5	3.6×10^{-3}	2.1×10^{-3}	2.6×10^{-2}	1.6×10^{-2}	0.26	0.13
1×10^6	3×10^5	3.7×10^{-3}	2.2×10^{-3}	1.9×10^{-2}	1.2×10^{-2}	0.16	7.3×10^{-2}
1×10^6	1×10^6	3.6×10^{-3}	2.5×10^{-3}	2.8×10^{-2}	1.7×10^{-2}	0.54	0.22
3×10^6	3×10^5	5.1×10^{-3}	2.7×10^{-3}	4.5×10^{-2}	2.4×10^{-2}	0.59	0.21
3×10^6	1×10^6	6.0×10^{-3}	2.9×10^{-3}	3.5×10^{-2}	1.7×10^{-2}	0.24	0.1
3×10^6	3×10^6	1.6×10^{-2}	7.5×10^{-3}	0.16	5.6×10^{-2}	2.6	0.56
1×10^7	1×10^6	1.9×10^{-2}	4.8×10^{-3}	0.2	5.7×10^{-2}	1.9	0.37
1×10^7	3×10^6	2.2×10^{-2}	5.1×10^{-3}	0.15	3.5×10^{-2}	1.3	0.26
1×10^7	1×10^7	0.6	7.8×10^{-2}	4.1	0.47	26	3.3
3×10^7	3×10^6	0.39	2.5×10^{-2}	3.7	0.24	37	1.8
3×10^7	1×10^7	2.4	3.7×10^{-2}	14	0.3	70	1.7
3×10^7	3×10^7	17	3.5	84	12	1.3×10^3	88
1×10^8	1×10^7	∞	3.3	∞	25	∞	130
1×10^8	3×10^7	∞	27	∞	130	∞	1.2×10^3

TABLE VIII: Median, 5% and 95% quantiles of the estimated measurement errors on χ_2 for different mass configurations at redshift $z = 1$ without considering alternative theory parameters.

$m_1[M_\odot]$	$m_2[M_\odot]$	$\Delta\chi_2$ without corrections					
		5%-quantile		Median		95%-quantile	
		RWF	FWF	RWF	FWF	RWF	FWF
3×10^5	3×10^4	8.3×10^{-4}	5.0×10^{-4}	2.7×10^{-3}	1.7×10^{-3}	1.9×10^{-2}	1.9×10^{-2}
3×10^5	1×10^5	7.4×10^{-4}	4.9×10^{-4}	3.4×10^{-3}	2.0×10^{-3}	2.0×10^{-2}	2.0×10^{-2}
3×10^5	3×10^5	9.0×10^{-4}	7.0×10^{-4}	6.6×10^{-3}	3.7×10^{-3}	7.6×10^{-2}	7.6×10^{-2}
1×10^6	1×10^5	1.8×10^{-3}	8.2×10^{-4}	5.6×10^{-3}	3.0×10^{-3}	3.5×10^{-2}	3.5×10^{-2}
1×10^6	3×10^5	1.4×10^{-3}	9.0×10^{-4}	4.8×10^{-3}	2.8×10^{-3}	3.5×10^{-2}	3.5×10^{-2}
1×10^6	1×10^6	1.5×10^{-3}	1.1×10^{-3}	1.1×10^{-2}	6.2×10^{-3}	0.18	0.18
3×10^6	3×10^5	2.2×10^{-3}	1.1×10^{-3}	7.4×10^{-3}	3.8×10^{-3}	5.9×10^{-2}	5.9×10^{-2}
3×10^6	1×10^6	2.1×10^{-3}	1.2×10^{-3}	7.5×10^{-3}	3.6×10^{-3}	4.8×10^{-2}	4.8×10^{-2}
3×10^6	3×10^6	4.6×10^{-3}	2.5×10^{-3}	4.1×10^{-2}	1.5×10^{-2}	0.68	0.68
1×10^7	1×10^6	6.4×10^{-3}	2.0×10^{-3}	3.4×10^{-2}	9.4×10^{-3}	0.19	0.19
1×10^7	3×10^6	7.4×10^{-3}	2.4×10^{-3}	3.2×10^{-2}	9.3×10^{-3}	0.18	0.18
1×10^7	1×10^7	0.12	2.2×10^{-2}	1.1	0.13	9.8	9.8
3×10^7	3×10^6	0.16	1.0×10^{-2}	1.4	6.5×10^{-2}	7.0	7.0
3×10^7	1×10^7	0.53	1.7×10^{-2}	4.3	9.8×10^{-2}	23	23
3×10^7	3×10^7	16	1.4	70	4.3	910	910
1×10^8	1×10^7	∞	1.5	∞	12	∞	∞
1×10^8	3×10^7	∞	11	∞	53	∞	∞

TABLE IX: Median, 5% and 95% quantiles of the estimated measurement errors on $2a$ for different mass configurations at redshift $z = 1$ with alternative theory parameters included.

$m_1[M_\odot]$	$m_2[M_\odot]$	$2a[']$ with corrections					
		5%-quantile		Median		95%-quantile	
		RWF	FWF	RWF	FWF	RWF	FWF
3×10^5	3×10^4	7.8	4.8	24	16	92	74
3×10^5	1×10^5	5.1	3.2	23	15	100	86
3×10^5	3×10^5	6.9	4.5	32	24	130	110
1×10^6	1×10^5	11	7.9	35	20	140	92
1×10^6	3×10^5	11	7.3	36	24	140	100
1×10^6	1×10^6	11	7.3	46	31	190	150
3×10^6	3×10^5	13	7.3	41	22	140	87
3×10^6	1×10^6	13	6.6	47	25	220	130
3×10^6	3×10^6	15	7.6	77	41	400	229
1×10^7	1×10^6	28	9.1	81	26	459	130
1×10^7	3×10^6	24	8.4	120	41	800	200
1×10^7	1×10^7	57	18	440	120	3.6×10^3	750
3×10^7	3×10^6	170	25	630	75	6.8×10^3	310
3×10^7	1×10^7	409	38	4.4×10^3	190	6.3×10^4	1.2×10^3
3×10^7	3×10^7	1.1×10^4	590	4.0×10^5	4.9×10^3	1.3×10^7	3.0×10^4
1×10^8	1×10^7	∞	2.2×10^3	∞	8.2×10^3	∞	4.3×10^4
1×10^8	3×10^7	∞	1.6×10^4	∞	8.3×10^4	∞	7.0×10^5

TABLE X: Median, 5% and 95% quantiles of the estimated measurement errors on $2a$ for different mass configurations at redshift $z = 1$ without considering alternative theory parameters.

$m_1[M_\odot]$	$m_2[M_\odot]$	$2a[']$ without corrections					
		5%-quantile		Median		95%-quantile	
		RWF	FWF	RWF	FWF	RWF	FWF
3×10^5	3×10^4	7.4	4.6	22	14	86	86
3×10^5	1×10^5	4.7	2.9	20	13	97	97
3×10^5	3×10^5	6.0	3.9	27	20	110	110
1×10^6	1×10^5	7.5	6.7	32	18	130	130
1×10^6	3×10^5	9.0	6.7	33	22	130	130
1×10^6	1×10^6	8.6	6.2	40	26	160	160
3×10^6	3×10^5	7.2	5.0	36	20	130	130
3×10^6	1×10^6	11	5.8	38	21	160	160
3×10^6	3×10^6	10	5.3	53	29	280	280
1×10^7	1×10^6	18	8.2	61	23	280	280
1×10^7	3×10^6	20	7.5	89	31	420	420
1×10^7	1×10^7	33	13	200	76	1.4×10^3	1.4×10^3
3×10^7	3×10^6	100	21	370	60	2.8×10^3	2.8×10^3
3×10^7	1×10^7	160	27	1.3×10^3	130	1.3×10^4	1.3×10^4
3×10^7	3×10^7	3.9×10^3	420	1.6×10^5	2.7×10^3	2.3×10^6	2.3×10^6
1×10^8	1×10^7	∞	1.2×10^3	∞	4.5×10^3	∞	∞
1×10^8	3×10^7	∞	7.2×10^3	∞	3.5×10^4	∞	∞

TABLE XI: Median, 5% and 95% quantiles of the estimated measurement errors on $2b$ for different mass configurations at redshift $z = 1$ with alternative theory parameters included.

$m_1[M_\odot]$	$m_2[M_\odot]$	$2b[']$ with corrections					
		5%-quantile		Median		95%-quantile	
		RWF	FWF	RWF	FWF	RWF	FWF
3×10^5	3×10^4	1.0	0.59	4.8	2.8	14	7.5
3×10^5	1×10^5	0.86	0.49	4.2	2.4	20	11
3×10^5	3×10^5	1.3	0.77	6.3	3.9	24	17
1×10^6	1×10^5	2.3	1.0	11	5.0	26	11
1×10^6	3×10^5	2.1	1.2	9.1	4.9	28	17
1×10^6	1×10^6	1.9	1.1	9.2	5.6	33	23
3×10^6	3×10^5	2.0	0.93	10	4.9	30	14
3×10^6	1×10^6	2.0	0.95	9.3	4.5	33	16
3×10^6	3×10^6	2.2	1.0	12	5.6	52	27
1×10^7	1×10^6	3.1	1.1	17	5.4	72	18
1×10^7	3×10^6	4.0	1.4	18	6.1	83	25
1×10^7	1×10^7	13	4.0	60	17	320	89
3×10^7	3×10^6	33	4.2	120	15	810	55
3×10^7	1×10^7	82	9.3	520	29	5.7×10^3	130
3×10^7	3×10^7	1.1×10^3	98	3.0×10^4	560	8.9×10^5	2.6×10^3
1×10^8	1×10^7	∞	459	∞	1.7×10^3	∞	7.1×10^3
1×10^8	3×10^7	∞	2.8×10^3	∞	1.3×10^4	∞	1.0×10^5

TABLE XII: Median, 5% and 95% quantiles of the estimated measurement errors on $2b$ for different mass configurations at redshift $z = 1$ without considering alternative theory parameters.

$m_1[M_\odot]$	$m_2[M_\odot]$	$2b[']$ without corrections					
		5%-quantile		Median		95%-quantile	
		RWF	FWF	RWF	FWF	RWF	FWF
3×10^5	3×10^4	0.97	0.56	4.6	2.6	13	13
3×10^5	1×10^5	0.74	0.43	3.9	2.2	17	17
3×10^5	3×10^5	1.1	0.65	5.6	3.2	20	20
1×10^6	1×10^5	2.1	0.94	10	4.6	25	25
1×10^6	3×10^5	2.0	1.0	8.7	4.6	25	25
1×10^6	1×10^6	1.7	0.96	8.4	4.9	29	29
3×10^6	3×10^5	1.8	0.85	9.8	4.6	26	26
3×10^6	1×10^6	1.6	0.85	8.4	4.0	28	28
3×10^6	3×10^6	1.5	0.77	9.5	4.6	39	39
1×10^7	1×10^6	2.7	0.87	14	4.8	45	45
1×10^7	3×10^6	3.1	1.1	14	4.9	57	57
1×10^7	1×10^7	6.2	2.1	26	9.8	120	120
3×10^7	3×10^6	16	2.7	65	12	290	290
3×10^7	1×10^7	40	4.2	150	16	910	910
3×10^7	3×10^7	540	49	4.8×10^3	260	1.6×10^5	1.6×10^5
1×10^8	1×10^7	∞	260	∞	900	∞	∞
1×10^8	3×10^7	∞	1.4×10^3	∞	4.9×10^3	∞	∞

TABLE XIII: Median, 5% and 95% quantiles of the estimated measurement errors on d_L for different mass configurations at redshift $z = 1$ with alternative theory parameters included.

$m_1[M_\odot]$	$m_2[M_\odot]$	$\Delta d_L/d_L$ with corrections					
		5%-quantile		Median		95%-quantile	
		RWF	FWF	RWF	FWF	RWF	FWF
3×10^5	3×10^4	2.6×10^{-3}	1.6×10^{-3}	5.0×10^{-3}	3.1×10^{-3}	1.5×10^{-2}	9.2×10^{-3}
3×10^5	1×10^5	2.2×10^{-3}	1.5×10^{-3}	5.1×10^{-3}	3.4×10^{-3}	1.7×10^{-2}	1.2×10^{-2}
3×10^5	3×10^5	2.6×10^{-3}	1.8×10^{-3}	7.4×10^{-3}	5.3×10^{-3}	2.2×10^{-2}	1.8×10^{-2}
1×10^6	1×10^5	3.8×10^{-3}	2.4×10^{-3}	7.9×10^{-3}	5.1×10^{-3}	2.3×10^{-2}	1.3×10^{-2}
1×10^6	3×10^5	3.2×10^{-3}	2.5×10^{-3}	7.3×10^{-3}	5.0×10^{-3}	2.5×10^{-2}	1.6×10^{-2}
1×10^6	1×10^6	3.8×10^{-3}	2.5×10^{-3}	1.0×10^{-2}	7.3×10^{-3}	3.0×10^{-2}	2.3×10^{-2}
3×10^6	3×10^5	4.6×10^{-3}	3.0×10^{-3}	9.8×10^{-3}	6.1×10^{-3}	2.9×10^{-2}	1.7×10^{-2}
3×10^6	1×10^6	5.2×10^{-3}	3.4×10^{-3}	1.2×10^{-2}	7.4×10^{-3}	3.5×10^{-2}	2.0×10^{-2}
3×10^6	3×10^6	7.5×10^{-3}	4.6×10^{-3}	2.3×10^{-2}	1.3×10^{-2}	8.0×10^{-2}	4.2×10^{-2}
1×10^7	1×10^6	1.4×10^{-2}	5.9×10^{-3}	3.6×10^{-2}	1.4×10^{-2}	0.12	3.2×10^{-2}
1×10^7	3×10^6	2.6×10^{-2}	7.9×10^{-3}	6.9×10^{-2}	1.7×10^{-2}	0.22	4.5×10^{-2}
1×10^7	1×10^7	0.23	4.4×10^{-2}	0.7	9.3×10^{-2}	3.2	0.25
3×10^7	3×10^6	0.97	3.8×10^{-2}	4.5	8.0×10^{-2}	23	0.19
3×10^7	1×10^7	8.5	0.11	40	0.27	200	0.71
3×10^7	3×10^7	630	5.1	1.7×10^4	12	2.9×10^5	52
1×10^8	1×10^7	∞	17	∞	73	∞	440
1×10^8	3×10^7	∞	170	∞	819	∞	1.7×10^4

TABLE XIV: Median, 5% and 95% quantiles of the estimated measurement errors on d_L for different mass configurations at redshift $z = 1$ without considering alternative theory parameters.

$m_1[M_\odot]$	$m_2[M_\odot]$	$\Delta d_L/d_L$ without corrections					
		5%-quantile		Median		95%-quantile	
		RWF	FWF	RWF	FWF	RWF	FWF
3×10^5	3×10^4	1.2×10^{-3}	8.1×10^{-4}	2.7×10^{-3}	1.6×10^{-3}	1.2×10^{-2}	1.2×10^{-2}
3×10^5	1×10^5	8.7×10^{-4}	5.6×10^{-4}	2.8×10^{-3}	1.7×10^{-3}	1.4×10^{-2}	1.4×10^{-2}
3×10^5	3×10^5	1.2×10^{-3}	7.3×10^{-4}	4.5×10^{-3}	2.9×10^{-3}	1.7×10^{-2}	1.7×10^{-2}
1×10^6	1×10^5	1.9×10^{-3}	9.5×10^{-4}	4.9×10^{-3}	2.4×10^{-3}	1.9×10^{-2}	1.9×10^{-2}
1×10^6	3×10^5	1.8×10^{-3}	1.1×10^{-3}	5.0×10^{-3}	2.9×10^{-3}	2.1×10^{-2}	2.1×10^{-2}
1×10^6	1×10^6	1.8×10^{-3}	1.2×10^{-3}	6.2×10^{-3}	4.0×10^{-3}	2.4×10^{-2}	2.4×10^{-2}
3×10^6	3×10^5	1.8×10^{-3}	1.0×10^{-3}	5.1×10^{-3}	2.6×10^{-3}	2.1×10^{-2}	2.1×10^{-2}
3×10^6	1×10^6	2.0×10^{-3}	1.1×10^{-3}	5.8×10^{-3}	3.2×10^{-3}	2.2×10^{-2}	2.2×10^{-2}
3×10^6	3×10^6	2.1×10^{-3}	1.4×10^{-3}	8.3×10^{-3}	4.7×10^{-3}	4.6×10^{-2}	4.6×10^{-2}
1×10^7	1×10^6	2.8×10^{-3}	1.3×10^{-3}	8.1×10^{-3}	3.3×10^{-3}	3.9×10^{-2}	3.9×10^{-2}
1×10^7	3×10^6	4.1×10^{-3}	2.2×10^{-3}	1.1×10^{-2}	4.7×10^{-3}	6.6×10^{-2}	6.6×10^{-2}
1×10^7	1×10^7	1.4×10^{-2}	7.3×10^{-3}	6.1×10^{-2}	2.1×10^{-2}	0.27	0.27
3×10^7	3×10^6	3.0×10^{-2}	5.0×10^{-3}	7.9×10^{-2}	1.1×10^{-2}	0.48	0.48
3×10^7	1×10^7	0.21	1.6×10^{-2}	0.75	3.3×10^{-2}	3.1	3.1
3×10^7	3×10^7	3.0	0.23	30	0.56	390	390
1×10^8	1×10^7	∞	0.41	∞	1.1	∞	∞
1×10^8	3×10^7	∞	3.4	∞	9.9	∞	∞

TABLE XV: Median, 5% and 95% quantiles of the estimated measurement errors on Ψ_{-1} for different mass configurations at redshift $z = 1$.

$m_1[M_\odot]$	$m_2[M_\odot]$	$\Delta\Psi_{-1}$					
		5%-quantile		Median		95%-quantile	
		RWF	FWF	RWF	FWF	RWF	FWF
3×10^5	3×10^4	3.0×10^{-6}	1.6×10^{-6}	7.2×10^{-6}	5.3×10^{-6}	6.5×10^{-5}	5.0×10^{-5}
3×10^5	1×10^5	2.9×10^{-6}	1.8×10^{-6}	7.7×10^{-6}	5.8×10^{-6}	6.1×10^{-5}	5.2×10^{-5}
3×10^5	3×10^5	5.3×10^{-6}	3.1×10^{-6}	1.6×10^{-5}	1.1×10^{-5}	1.8×10^{-4}	1.3×10^{-4}
1×10^6	1×10^5	1.5×10^{-5}	6.9×10^{-6}	3.5×10^{-5}	2.2×10^{-5}	3.3×10^{-4}	2.4×10^{-4}
1×10^6	3×10^5	1.5×10^{-5}	7.8×10^{-6}	3.5×10^{-5}	2.6×10^{-5}	2.7×10^{-4}	1.8×10^{-4}
1×10^6	1×10^6	5.1×10^{-5}	2.2×10^{-5}	1.4×10^{-4}	8.7×10^{-5}	7.7×10^{-4}	5.0×10^{-4}
3×10^6	3×10^5	9.8×10^{-5}	2.5×10^{-5}	2.0×10^{-4}	1.1×10^{-4}	1.2×10^{-3}	6.4×10^{-4}
3×10^6	1×10^6	2.0×10^{-4}	6.6×10^{-5}	4.0×10^{-4}	1.7×10^{-4}	1.1×10^{-3}	6.4×10^{-4}
3×10^6	3×10^6	8.8×10^{-4}	2.0×10^{-4}	2.6×10^{-3}	7.5×10^{-4}	8.7×10^{-3}	2.4×10^{-3}
1×10^7	1×10^6	2.6×10^{-3}	3.1×10^{-4}	6.3×10^{-3}	9.0×10^{-4}	1.9×10^{-2}	3.0×10^{-3}
1×10^7	3×10^6	6.9×10^{-3}	1.1×10^{-3}	1.9×10^{-2}	2.0×10^{-3}	5.6×10^{-2}	4.8×10^{-3}
1×10^7	1×10^7	6.2×10^{-2}	9.8×10^{-3}	0.18	2.5×10^{-2}	0.77	6.0×10^{-2}
3×10^7	3×10^6	0.28	8.9×10^{-3}	1.4	1.7×10^{-2}	8.1	5.1×10^{-2}
3×10^7	1×10^7	2.3	3.6×10^{-2}	14	0.1	71	0.27
3×10^7	3×10^7	190	1.7	5.9×10^3	4.1	1.1×10^5	17
1×10^8	1×10^7	∞	4.6	∞	22	∞	170
1×10^8	3×10^7	∞	55	∞	280	∞	6.1×10^3

TABLE XVI: Median, 5% and 95% quantiles of the estimated measurement errors on Ψ_0 for different mass configurations at redshift $z = 1$.

$m_1[M_\odot]$	$m_2[M_\odot]$	$\Delta\Psi_0$					
		5%-quantile		Median		95%-quantile	
		RWF	FWF	RWF	FWF	RWF	FWF
3×10^5	3×10^4	1.5×10^{-3}	7.4×10^{-4}	3.2×10^{-3}	2.1×10^{-3}	1.7×10^{-2}	1.2×10^{-2}
3×10^5	1×10^5	1.3×10^{-3}	7.2×10^{-4}	3.3×10^{-3}	2.3×10^{-3}	1.7×10^{-2}	1.4×10^{-2}
3×10^5	3×10^5	2.3×10^{-3}	1.4×10^{-3}	6.1×10^{-3}	4.5×10^{-3}	4.3×10^{-2}	3.2×10^{-2}
1×10^6	1×10^5	4.8×10^{-3}	1.9×10^{-3}	1.1×10^{-2}	6.3×10^{-3}	7.0×10^{-2}	4.7×10^{-2}
1×10^6	3×10^5	4.9×10^{-3}	2.4×10^{-3}	1.1×10^{-2}	7.8×10^{-3}	6.1×10^{-2}	4.1×10^{-2}
1×10^6	1×10^6	1.4×10^{-2}	5.2×10^{-3}	3.8×10^{-2}	2.3×10^{-2}	0.16	0.11
3×10^6	3×10^5	2.1×10^{-2}	4.4×10^{-3}	4.5×10^{-2}	2.4×10^{-2}	0.21	0.11
3×10^6	1×10^6	3.8×10^{-2}	1.1×10^{-2}	8.4×10^{-2}	3.6×10^{-2}	0.21	0.12
3×10^6	3×10^6	0.13	2.2×10^{-2}	0.38	0.12	1.3	0.37
1×10^7	1×10^6	0.3	3.5×10^{-2}	0.75	0.14	2.4	0.43
1×10^7	3×10^6	0.7	0.12	2.0	0.27	6.0	0.67
1×10^7	1×10^7	4.9	0.96	14	2.4	60	6.2
3×10^7	3×10^6	9.8	0.78	76	1.8	590	4.9
3×10^7	1×10^7	88	2.7	720	8.9	4.3×10^3	25
3×10^7	3×10^7	3.8×10^3	120	1.7×10^5	300	6.2×10^6	1.5×10^3
1×10^8	1×10^7	∞	150	∞	980	∞	1.1×10^4
1×10^8	3×10^7	∞	2.1×10^3	∞	1.4×10^4	∞	4.1×10^5

TABLE XVII: Median, 5% and 95% quantiles of the estimated measurement errors on $\Psi_{1/2}$ for different mass configurations at redshift $z = 1$.

$m_1[M_\odot]$	$m_2[M_\odot]$	$\Delta\Psi_{1/2}$					
		5%-quantile		Median		95%-quantile	
		RWF	FWF	RWF	FWF	RWF	FWF
3×10^5	3×10^4	1.6×10^{-2}	5.8×10^{-3}	3.7×10^{-2}	2.0×10^{-2}	0.14	0.11
3×10^5	1×10^5	1.3×10^{-2}	7.0×10^{-3}	3.4×10^{-2}	2.3×10^{-2}	0.14	0.11
3×10^5	3×10^5	1.8×10^{-2}	1.1×10^{-2}	5.3×10^{-2}	4.0×10^{-2}	0.29	0.21
1×10^6	1×10^5	4.0×10^{-2}	1.5×10^{-2}	9.1×10^{-2}	5.0×10^{-2}	0.45	0.3
1×10^6	3×10^5	3.7×10^{-2}	1.9×10^{-2}	8.7×10^{-2}	6.2×10^{-2}	0.42	0.28
1×10^6	1×10^6	9.8×10^{-2}	3.7×10^{-2}	0.27	0.16	0.98	0.7
3×10^6	3×10^5	0.12	3.1×10^{-2}	0.29	0.15	1.2	0.65
3×10^6	1×10^6	0.23	7.2×10^{-2}	0.51	0.23	1.3	0.73
3×10^6	3×10^6	0.66	0.12	2.0	0.64	6.6	2.1
1×10^7	1×10^6	1.3	0.17	3.6	0.75	12	2.4
1×10^7	3×10^6	3.0	0.55	9.0	1.3	29	3.5
1×10^7	1×10^7	19	4.1	55	10	240	29
3×10^7	3×10^6	23	3.1	250	7.8	2.1×10^3	23
3×10^7	1×10^7	150	10	2.3×10^3	37	1.4×10^4	110
3×10^7	3×10^7	1.2×10^4	430	3.4×10^5	1.1×10^3	7.7×10^6	6.4×10^3
1×10^8	1×10^7	∞	320	∞	2.9×10^3	∞	4.1×10^4
1×10^8	3×10^7	∞	4.5×10^3	∞	4.5×10^4	∞	1.4×10^6

TABLE XVIII: Median, 5% and 95% quantiles of the estimated measurement errors on Ψ_1 for different mass configurations at redshift $z = 1$.

$m_1[M_\odot]$	$m_2[M_\odot]$	5%-quantile		$\Delta\Psi_1$ Median		95%-quantile	
		RWF	FWF	RWF	FWF	RWF	FWF
3×10^5	3×10^4	0.15	3.5×10^{-2}	0.33	0.17	0.92	0.64
3×10^5	1×10^5	0.14	4.7×10^{-2}	0.34	0.2	0.95	0.79
3×10^5	3×10^5	0.19	6.8×10^{-2}	0.49	0.29	1.7	1.3
1×10^6	1×10^5	0.3	7.9×10^{-2}	0.65	0.34	2.1	1.3
1×10^6	3×10^5	0.29	0.11	0.64	0.41	1.9	1.4
1×10^6	1×10^6	0.47	0.13	1.2	0.65	3.7	2.8
3×10^6	3×10^5	0.61	0.13	1.4	0.7	4.1	2.2
3×10^6	1×10^6	0.78	0.21	1.8	0.86	4.7	2.5
3×10^6	3×10^6	1.3	0.29	4.0	1.4	16	6.1
1×10^7	1×10^6	3.0	0.36	8.8	2.3	30	5.8
1×10^7	3×10^6	5.1	0.92	14	2.6	45	7.2
1×10^7	1×10^7	26	5.7	76	13	330	35
3×10^7	3×10^6	58	6.6	570	16	4.0×10^3	38
3×10^7	1×10^7	409	15	3.3×10^3	46	1.9×10^4	120
3×10^7	3×10^7	2.1×10^4	459	4.3×10^5	1.2×10^3	2.1×10^7	5.0×10^3
1×10^8	1×10^7	∞	919	∞	6.7×10^3	∞	6.8×10^4
1×10^8	3×10^7	∞	7.8×10^3	∞	5.9×10^4	∞	1.4×10^6

TABLE XIX: Median, 5% and 95% quantiles of the estimated measurement errors on $\Psi_{3/2}$ for different mass configurations at redshift $z = 1$.

$m_1[M_\odot]$	$m_2[M_\odot]$	5%-quantile		$\Delta\Psi_{3/2}$ Median		95%-quantile	
		RWF	FWF	RWF	FWF	RWF	FWF
3×10^5	3×10^4	1.1	0.16	2.5	1.5	8.0	5.7
3×10^5	1×10^5	1.3	0.18	3.1	1.8	9.1	7.3
3×10^5	3×10^5	2.0	0.3	5.3	2.9	18	14
1×10^6	1×10^5	2.9	0.33	6.3	3.5	25	17
1×10^6	3×10^5	3.2	0.44	7.1	4.5	24	16
1×10^6	1×10^6	6.7	0.85	17	8.6	44	32
3×10^6	3×10^5	7.6	0.48	17	9.1	54	28
3×10^6	1×10^6	11	1.4	26	12	67	35
3×10^6	3×10^6	20	1.7	54	19	170	71
1×10^7	1×10^6	32	2.7	110	32	360	81
1×10^7	3×10^6	56	11	180	37	590	100
1×10^7	1×10^7	250	61	770	150	3.6×10^3	459
3×10^7	3×10^6	459	71	4.0×10^3	190	3.4×10^4	490
3×10^7	1×10^7	2.9×10^3	140	2.4×10^4	490	1.4×10^5	1.5×10^3
3×10^7	3×10^7	1.3×10^5	3.2×10^3	2.4×10^6	1.1×10^4	6.4×10^7	6.8×10^4
1×10^8	1×10^7	∞	8.4×10^3	∞	4.4×10^4	∞	5.9×10^5
1×10^8	3×10^7	∞	6.0×10^4	∞	4.5×10^5	∞	1.4×10^7

TABLE XX: Median, 5% and 95% quantiles of the estimated measurement errors on Ψ_2 for different mass configurations at redshift $z = 1$.

$m_1[M_\odot]$	$m_2[M_\odot]$	5%-quantile		$\Delta\Psi_2$ Median		95%-quantile	
		RWF	FWF	RWF	FWF	RWF	FWF
3×10^5	3×10^4	4.0	0.36	9.1	5.5	30	21
3×10^5	1×10^5	5.0	0.45	12	7.1	36	28
3×10^5	3×10^5	8.2	0.86	21	12	71	50
1×10^6	1×10^5	11	0.98	24	13	88	59
1×10^6	3×10^5	13	1.7	28	17	89	60
1×10^6	1×10^6	26	2.9	65	32	170	110
3×10^6	3×10^5	26	1.1	62	32	190	96
3×10^6	1×10^6	39	3.8	95	42	240	120
3×10^6	3×10^6	60	5.4	170	61	570	240
1×10^7	1×10^6	79	7.7	310	100	1.1×10^3	250
1×10^7	3×10^6	130	30	459	110	1.5×10^3	320
1×10^7	1×10^7	480	130	1.6×10^3	350	8.1×10^3	1.1×10^3
3×10^7	3×10^6	969	200	8.1×10^3	500	6.7×10^4	1.4×10^3
3×10^7	1×10^7	8.5×10^3	390	4.2×10^4	969	2.4×10^5	2.9×10^3
3×10^7	3×10^7	1.5×10^5	6.7×10^3	4.1×10^6	1.8×10^4	8.9×10^7	1.3×10^5
1×10^8	1×10^7	∞	2.5×10^4	∞	1.1×10^5	∞	1.1×10^6
1×10^8	3×10^7	∞	1.5×10^5	∞	8.5×10^5	∞	2.2×10^7

-
- [1] C. M. Will, Living Reviews in Relativity **9** (2006), arXiv:gr-qc/0510072.
 - [2] C. Brans and R. H. Dicke, Phys. Rev. **124**, 925 (1961).
 - [3] J. Bekenstein and M. Milgrom, Astrophys. J. **286**, 7 (1984).
 - [4] J. D. Bekenstein, Phys. Rev. D **70**, 083509 (2004).
 - [5] V. Faraoni, ArXiv e-prints (2008), arXiv:0810.2602v1.
 - [6] C. M. Will, Phys. Rev. D **57**, 2061 (1998).
 - [7] A. Stavridis and C. M. Will, Phys. Rev. D **80**, 044002 (2009).
 - [8] N. Yunes and F. Pretorius, Phys. Rev. D **80**, 122003 (2009).
 - [9] ESA Science & Technology: Next steps for LISA (2011), URL <http://sci.esa.int/science-e/www/object/index.cfm?fobjectid=48728>.
 - [10] L. S. Finn, Phys. Rev. D **46**, 5236 (1992).
 - [11] E. Poisson and C. M. Will, Phys. Rev. D **52**, 848 (1995).
 - [12] C. M. Will, Phys. Rev. D **50**, 6058 (1994).
 - [13] P. D. Scharre and C. M. Will, Phys. Rev. D **65**, 042002 (2002).
 - [14] E. Berti, A. Buonanno, and C. M. Will, Phys. Rev. D **71**, 084025 (2005).
 - [15] K. Yagi and T. Tanaka, Phys. Rev. D **81**, 064008 (2010).
 - [16] K. G. Arun and C. M. Will, Classical and Quantum Gravity **26**, 155002 (2009).
 - [17] D. Keppel and P. Ajith, Phys. Rev. D **82**, 122001 (2010).
 - [18] E. Berti, J. Gair, and A. Sesana, ArXiv e-prints (2011), arXiv:1107.3528.
 - [19] K. G. Arun, B. R. Iyer, M. S. S. Qusailah, and B. S. Sathyaprakash, Classical and Quantum Gravity **23**, L37 (2006).
 - [20] N. Cornish, L. Sampson, N. Yunes, and F. Pretorius, ArXiv e-prints (2011), arXiv:1105.2088.
 - [21] L. Blanchet, Living Reviews in Relativity **9** (2006), arXiv:gr-qc/9903107.
 - [22] L. Blanchet, A. Buonanno, and G. Faye, Phys. Rev. D **74**, 104034 (2006).
 - [23] T. A. Apostolatos, C. Cutler, G. J. Sussman, and K. S. Thorne, Phys. Rev. D **49**, 6274 (1994).
 - [24] K. G. Arun, A. Buonanno, G. Faye, and E. Ochsner, Phys. Rev. D **79**, 104023 (2009).
 - [25] E. Komatsu, J. Dunkley, M. R. Nolte, C. L. Bennett, B. Gold, G. Hinshaw, N. Jarosik, D. Larson, M. Limon, L. Page, et al., Astrophysical Journal Supplement Series **180**, 330 (2009).
 - [26] C. M. Will, *Theory and Experiment in Gravitational Physics* (Cambridge University Press, Cambridge, England, 1993).
 - [27] K. S. Thorne, Reviews of Modern Physics **52**, 299 (1980).
 - [28] L. Blanchet, G. Faye, B. R. Iyer, and B. Joguet, Phys. Rev. D **65**, 061501 (2002).
 - [29] A. Klein, P. Jetzer, and M. Sereno, Phys. Rev. D **80**, 064027 (2009).
 - [30] N. Yunes, K. G. Arun, E. Berti, and C. M. Will, Phys. Rev. D **80**, 084001 (2009).
 - [31] S. Droz, D. J. Knapp, E. Poisson, and B. J. Owen, Phys. Rev. D **59**, 124016 (1999).
 - [32] C. Cutler and É. E. Flanagan, Phys. Rev. D **49**, 2658 (1994).
 - [33] M. Vallisneri, Phys. Rev. D **77**, 042001 (2008).
 - [34] T. B. Littenberg and N. J. Cornish, Phys. Rev. D **80**, 063007 (2009).
 - [35] K. G. Arun, S. Babak, E. Berti, N. Cornish, C. Cutler, J. Gair, S. A. Hughes, B. R. Iyer, R. N. Lang, I. Mandel, et al., Classical and Quantum Gravity **26**, 094027 (2009).
 - [36] R. N. Lang and S. A. Hughes, Phys. Rev. D **74**, 122001 (2006).
 - [37] S. Alexander and N. Yunes, Phys. Rep. **480**, 1 (2009).
 - [38] L. Blanchet, B. R. Iyer, and B. Joguet, Phys. Rev. D **65**, 064005 (2002).
 - [39] L. Blanchet, T. Damour, and G. Esposito-Farèse, Phys. Rev. D **69**, 124007 (2004).
 - [40] L. Blanchet, T. Damour, G. Esposito-Farèse, and B. R. Iyer, Phys. Rev. D **71**, 124004 (2005).